Earth and Planetary Science Letters 401 (2014) 215–226

Contents lists available at ScienceDirect

Earth and Planetary Science Letters

www.elsevier.com/locate/epsl

Complementary slip distributions of the August 4, 2003 M_w 7.6 and November 17, 2013 M_w 7.8 South Scotia Ridge earthquakes

Lingling Ye [a], Thorne Lay [a,*], Keith D. Koper [b], Robert Smalley Jr. [c], Luis Rivera [d], Michael G. Bevis [e], Andrés F. Zakrajsek [f], Felix Norman Teferle [g]

[a] Department of Earth and Planetary Sciences, University of California Santa Cruz, Santa Cruz, CA 95064, USA
[b] Department of Geology and Geophysics, University of Utah, Salt Lake City, UT 84112, USA
[c] Center for Earthquake Research and Information, The University of Memphis, Memphis, TN 38152, USA
[d] Institut de Physique du Globe de Strasbourg, Université de Strasbourg/CNRS, Strasbourg, France
[e] School of Earth Sciences, Ohio State University, 275 Mendenhall Laboratory, Columbus, OH 43210, USA
[f] Ciencias de la Tierra, Dirección Nacional del Antártico – Instituto Antártico Argentino, Argentina
[g] Geophysics Laboratory, University of Luxembourg, Luxembourg L-1359, Luxembourg

ARTICLE INFO

Article history:
Received 8 April 2014
Received in revised form 5 June 2014
Accepted 6 June 2014
Available online xxxx
Editor: P. Shearer

Keywords:
Scotia Plate earthquakes
strike-slip faulting
finite-fault models
fault asperities
high-rate GPS

ABSTRACT

The South Scotia Ridge Transform (SSRT) plate boundary between the Scotia and Antarctic plates experienced large strike-slip earthquakes on August 4, 2003 (M_w 7.6) and November 17, 2013 (M_w 7.8). These events have overlapping aftershock zones, which is unusual. A 36°–45° southward dipping fault zone ruptured with left-lateral displacements in each event along the northern margin of the South Orkney micro-continent near 60°S. Slip distributions for the two events are determined using teleseismic body and surface wave recordings along with constraints from GPS ground motion recordings at station BORC on Laurie Island (South Orkney Islands), just south of the SSRT. The aftershock distributions, high-frequency back-projections, and unconstrained body wave finite-fault inversions permit significant overlap of the 2003 and 2013 slip zones; however, the GPS static displacements resolve differences in the large-slip regions of the two ruptures. The 2013 earthquake sequence along the SSRT initiated with M_w 6.1 (November 13) and M_w 6.8 (November 16) foreshocks located ~50 km west of the mainshock hypocenter, and had aftershocks extending ~250 km eastward. The rupture spread primarily eastward at ~2.5 km/s with a total rupture duration of about 120 s, with two distinct patches of large-slip located northwest and northeast of the South Orkney Islands. The rupture swept past BORC, with high-rate GPS (HRGPS) ground motion recordings capturing the time-varying slip history of the faulting. Traditional GPS data require that the largest-slip region of the shorter rupture in 2003 is located in the gap NNE of BORC between the two patches that ruptured in 2013. There appears to be some overlap of lower slip regions. The complementary slip distributions comprise a relatively uniform offset along this portion of the SSRT, which is one of the most seismically active regions of the entire Antarctic plate boundary.

1. Introduction

Reconstruction of Scotia plate tectonic evolution includes a complicated tectonic history dating back to ~120 Ma, when fragmentation of Gondwanaland initiated differential motion between the South America and Antarctic plates (Dalziel et al., 2013). Subsequent seafloor spreading within what is now the Scotia plate dispersed and stretched continental fragments separated from southern South America and the Antarctic Peninsula during the past ~6–40 Ma. The eastern margin of the Scotia plate is the East Scotia Ridge (ESR). The ESR is an active back-arc spreading ridge associated with subduction of the South American plate beneath the South Sandwich plate along the South Sandwich subduction zone (Fig. 1). The North and South Scotia Ridge transforms (NSRT and SSRT), now trending roughly EW for ~1000–1500 km, formed at ~20–30 Ma, and are closely associated with spreading of the West Scotia Ridge (WSR), which ended ~6.6 Ma. These boundaries contain a mix of continental and oceanic crust (Civile et al., 2012; Martos et al., 2014), notably the South Georgia and South Orkney Islands along the NSRT and SSRT, respectively.

* Corresponding author. Tel.: +831 459 3164.
E-mail address: tlay@ucsc.edu (T. Lay).

http://dx.doi.org/10.1016/j.epsl.2014.06.007
0012-821X/

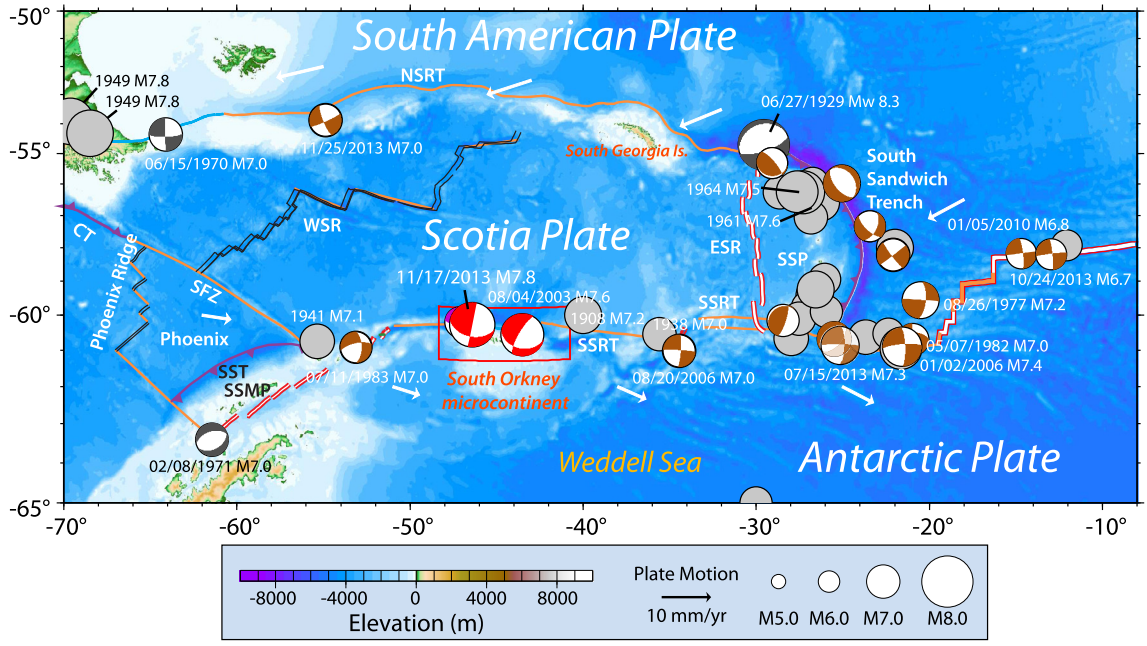

Fig. 1. Large earthquakes around the Scotia Plate with tectonic structures (after Dalziel et al., 2013). Gray circles indicate epicenters of $M_w \geq 7.0$ events from 1900 to 1975 from PAGER-CAT (Allen et al., 2009). Gray focal mechanisms for 1970 and 1971 events are from Pelayo and Wiens (1989) and that for the 1929 event is from Okal and Hartnady (2009). Brown focal mechanisms are global Centroid Moment Tensor (gCMT) solutions for $M_w \geq 6.5$ events from 1976 to 2014 plotted at the USGS/NEIC epicenters. The red mechanisms are the gCMT solution for the November 17, 2013 M_w 7.8 and August 4, 2003 M_w 7.6 events. Arrows indicate the plate motion directions and rates relative to a fixed Scotia Plate computed using model MORVEL (DeMets et al., 2010). Relative to the Scotia plate, the Antarctic Plate is moving at ~6–7 mm/yr eastward with minor tensional obliquity along the South Scotia Ridge transform (SSRT), and the South American Plate at ~8–9 mm/yr westward with minor compressional obliquity along the North Scotia Ridge transform (NSRT). The purple curves indicate subduction zones; orange lines show transforms and fracture zones; double red lines indicate the active spreading centers; and black double lines show extinct spreading centers. The West Scotia Ridge (WSR) and the Phoenix Ridge (Livermore et al., 1994, 2000) ceased spreading at approximate 6.5 Ma and 3.3 Ma, respectively. The East Scotia Ridge (ESR) initializes at ~9 Ma B.P., and its spreading rate is estimated to be ~6–7 cm/yr (Smalley et al., 2007; Thomas et al., 2003). The red box indicates the main study region (Fig. 8). Other abbreviations: CT, Chile Trench; SFZ, Shackleton Fracture Zone; SST, South Shetlands Trench; SSMP, South Shetlands microplate; SSP, South Sandwich Plate.

Kinematics of the Scotia plate, determined from magnetic lineations, earthquake slip vectors, transform azimuths, gravity anomalies, and GPS crustal velocities indicate that, with its internal structure now stabilized, the Scotia plate essentially serves as a large shear zone between the South America and Antarctic plates. The SSRT and NSRT, with left-lateral motions of ~6–7 mm/yr and ~8–9 mm/yr respectively, partition the total relative movement between the two large plates (DeMets et al., 2010; Forsyth, 1975; Pelayo and Wiens, 1989; Livermore et al., 1994; Smalley et al., 2007; Thomas et al., 2003). The SSRT is the most seismically active portion of the entire Antarctic plate boundary, having experienced about ten M_w 7+ events since 1908, whereas less seismicity and few large events have been recorded on the NSRT (Figs. 1, S1, S2 and S3). The NSRT and SSRT continue eastward past the ESR forming the northern and southern boundaries of the "D" shaped South Sandwich plate. The NSRT continuation turns southward and changes into the South Sandwich trench (SST) on the north, while the SSRT continuation bifurcates into the SST from the south and a further eastward continuation to form a strike-slip boundary between the Antarctic and South America plates. Additional large events are found on the continuation of the SSRT on the boundaries between the Antarctic and the South Sandwich and South American plates.

On November 17, 2013 (09:04:55 UTC, 60.27°S, 46.40°W; USGS-NEIC), an M_w 7.8 strike-slip earthquake occurred on the SSRT; the largest earthquake yet recorded along this plate boundary. The rupture initiated about 150 km west of the previous largest earthquake, an M_w 7.6 event on August 4, 2003 (04:37:23 UTC, 60.57°S, 43.50°W; USGS-NEIC). The eastern half of the 2013 aftershock zone overlaps that of the 2003 event (Fig. S1). Inversions of long-period seismic waves from gCMT (http://www.globalcmt.org/CMTsearch.html) and our own W-phase inversions noted below indicate left-lateral strike-slip displacements on faults striking 97°–102° and dipping 36°–63° southward for both events (Figs. 1 and S3). There are two unusual and surprising aspects of the earthquake: the shallow dip of the strike-slip faulting suggests reactivation of a thrust fault which may have formed due to compression from past convergence or continental fragmentation along the SSRT, and the short apparent time for re-rupture of the segment of the plate boundary that failed in 2003 (Vallée and Satriano, 2014). We analyze the rupture characteristics of these two large events to quantify the slip distribution and faulting processes along this complex plate boundary.

2. Rupture characteristics of the 2003 and 2013 events

The first-order characteristics of the faulting processes for the two large South Scotia Ridge earthquakes are determined using long-period point-source solutions, back-projection of short-period teleseismic P wave recordings, and surface wave directivity analysis for globally recorded digital seismograms.

2.1. Long-period point-source solutions

The long-period point-source moment-tensor best-double-couple solutions from gCMT and our W-phase inversions for both August 4, 2003 and November 17, 2013 events are listed in Table 1. The W-phase inversions use three-component long-period signals in the 1.67–5.0 mHz pasband from 29 stations with 50 total channels for the 2003 event, and 28 stations with 53 total channels for the 2013 event. Centroid depths less than 16 km are preferred for both events in the W-phase inversions. The

Table 1
Long-period point-source solutions.

Event	Type	M_0 (N-m)	Centroid time (s)	Depth (km)	Strike (°)	Dip (°)	Rake (°)
08/04/2003 Scotia event	gCMT	2.73×10^{20}	22.4	15.0	101	36	−23
	W-phase	1.85×10^{20}	15.0	15.5	103	63	−32
11/17/2013 Scotia event	gCMT	5.82×10^{20}	45.5	23.8	102	44	3
	W-phase	6.45×10^{20}	44.4	11.5	97	46	−3

6

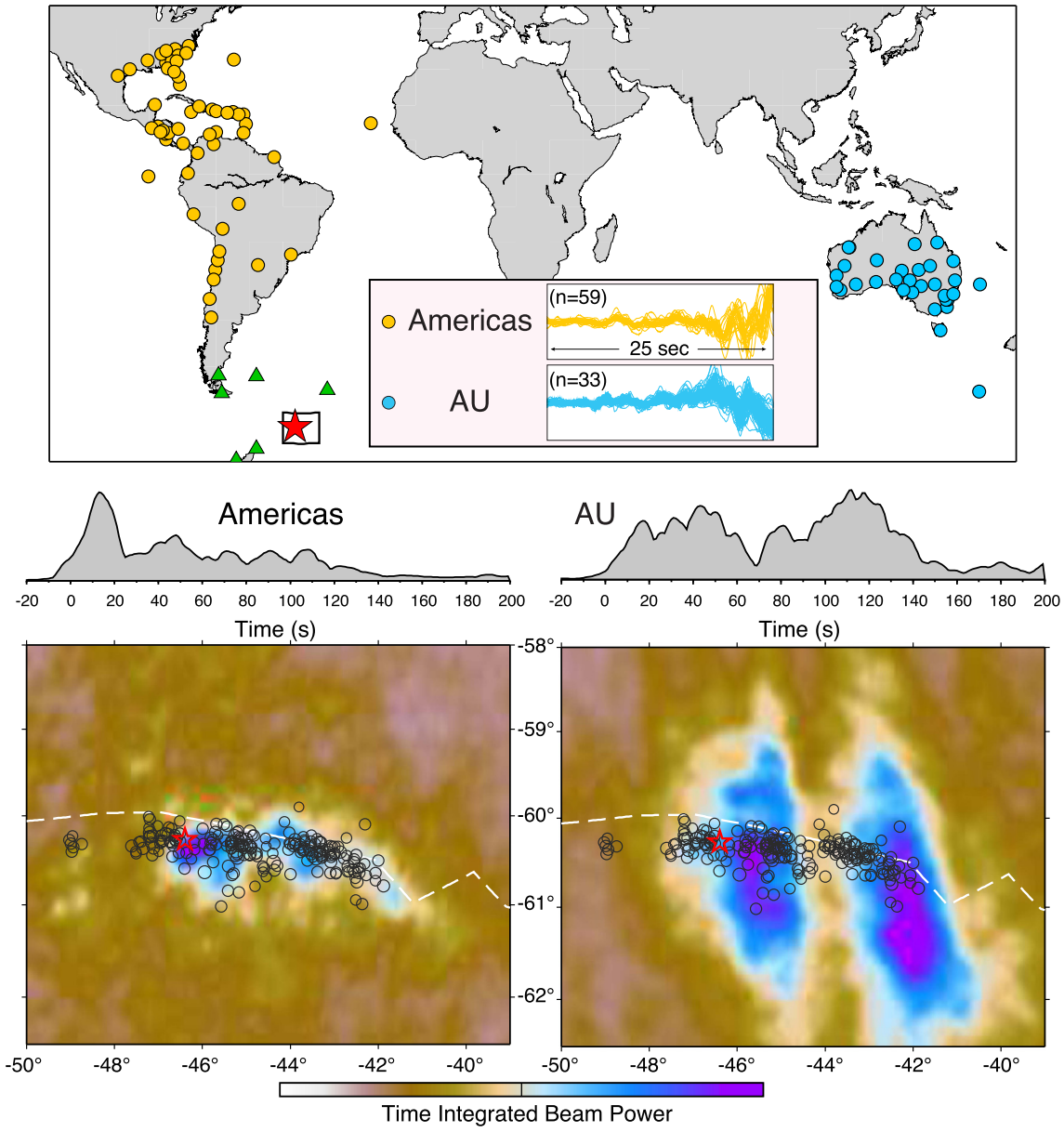

Fig. 2. Constraints on rupture velocity and rupture length from P wave back-projection. Teleseismic P waves (top panel inset) in the frequency band from 0.5 to 2.0 Hz from large networks (top panel) of stations in the Americas (gold) and Australia (AU) (blue), with the threshold of cross-correlation coefficient for the signals in inset of top panel of 0.6, were used to image the space–time history of coherent high frequency seismic radiation from the November 17, 2013 M_w 7.8 Scotia earthquake. The time-integrated power stacked on a source region grid from each network is shown in the lower panels relative to the mainshock epicenter (red star) and aftershock sequence (black circles). The time sequences of peak beam power are shown in the central panels. The darker blue and light purple colors indicate higher power of coherent energy release with eastward rupture expansion for over 250 km in the images from both networks. A rupture velocity of ~2.0–2.5 km/s is estimated from the space–time history of high-frequency radiation (see supplementary Fig. S4). Supplementary animations, Movies S1 and S2, show the time varying images throughout the rupture process for each network. The green triangles in the map show the location of the GPS sites used for calibrating the co-seismic HRGPS recording at BORC.

gCMT and W-phase solutions are very consistent for the 2013 event but differ by 27° in dip for the 2003 event. Differences in predicted W-phase waveforms and following fundamental mode surface wave arrivals are small for the range of dips listed in Table 1, so we prefer the gCMT dip for the 2003 event because more data are available for that inversion. Very steep dips, as might be expected for strike-slip events, are not consistent with the long-period data.

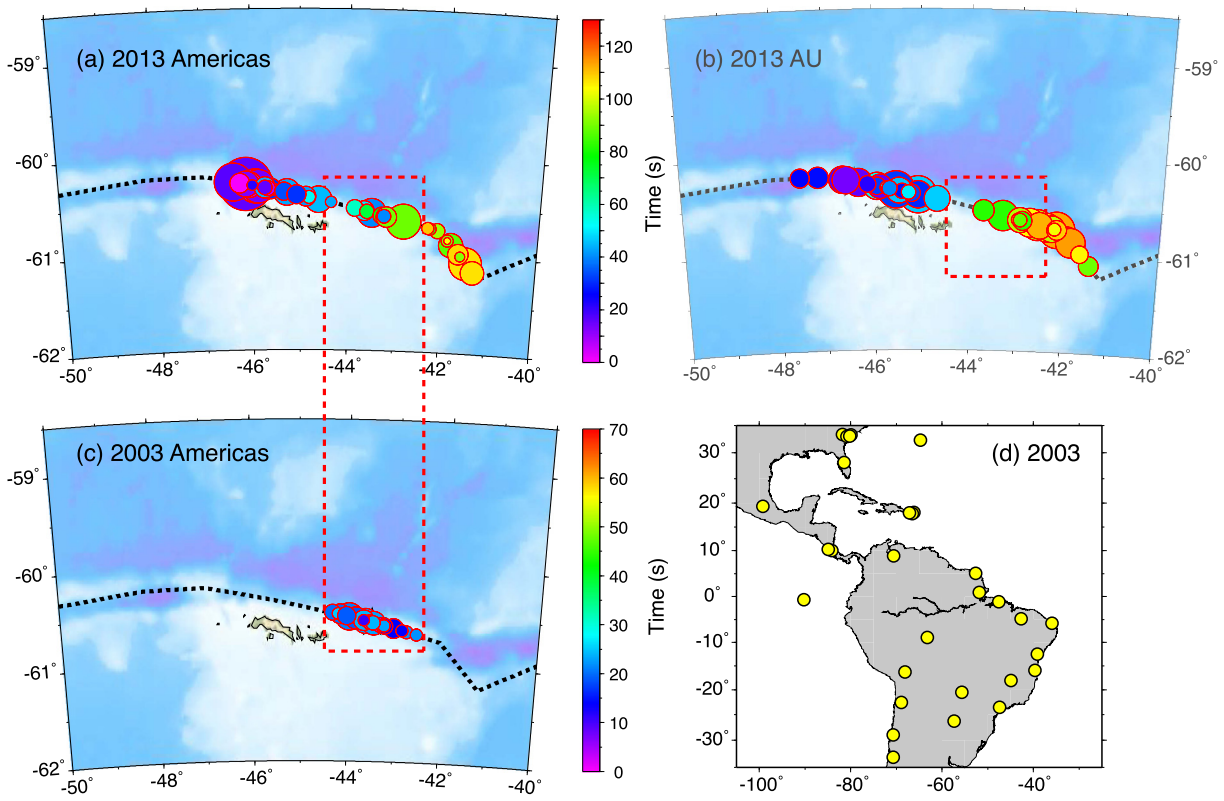

Fig. 3. The distribution of coherent teleseismic high-frequency (0.5–2.0 Hz) P wave energy obtained by deconvolving the P wave back-projection images from networks in the Americas and Australia (AU) by the corresponding array response functions at 1 Hz for the November 17, 2013 M_w 7.8 Scotia earthquake (a and b) and August 4, 2003 M_w 7.6 Scotia earthquake (c) constrained to rupture along the plate boundary (dashed black line). This procedure results in images of discrete bursts of coherent-energy radiation in time and space that are free of the smearing created by the array limitations. The networks used for the 2013 event are shown in Fig. 2, and the network in the Americas used for the 2003 event is shown in (d). The size of circles in (a), (b) and (c) indicates the relative amplitude after deconvolution, color-coded with the time after origin time. The dashed red box emphasizes the relative location of the coherent energy release of the 2013 and 2003 events. A rupture velocity along the plate boundary of ~2.0–3.0 km/s, is estimated for the 2013 event (see supplementary Fig. S5).

2.2. Back-projection analysis

Teleseismic short-period, 0.5–2.0 s, P wave recordings for the November 17, 2013 event from two large networks of stations in Australia (AU) and the Americas (Fig. 2) are used for back-projections to estimate the rupture speed (V_r) and length following the procedure described by Xu et al. (2009). While there are some differences in the back-projections for the two networks, both produce images with two loci of coherent short-period radiation eastward from the hypocenter. The first patch of radiation was released from 10–50 s after the origin time as the rupture extended ~100 km to the east and the secondary patch was released from ~70–100 s after the origin time as the rupture continued eastward another ~150–250 km (Fig. 2, Supplementary Animations S1, S2). There is a gap between the two regions of coherent short-period emissions. The AU data indicate somewhat longer duration of source radiation, with coherent energy out to ~130 s. The space–time patterns of the short-period radiation indicate a rupture velocity of about 2.0–2.5 km/s (Fig. S4). The image from the AU network is spatially less-well resolved overall in the north–south direction than that from the Americas, but provides better east–west separation of the two patches of strong radiation due to more favorable imaging geometry, and both images are blurred by typical network response distortion of the back-projection. Joint back-projection was not performed because the signal energy distribution differs for the events due to radiation pattern and different depth phase interference effects.

To suppress the blurring effects from the network limitations, we perform an iterative deconvolution of the back-projection images by the corresponding array response functions for a 1 s period impulse, constraining the solution to lie along the SSRT boundary. This deconvolution procedure follows that of Lay et al. (2009), and provides a parsimonious characterization of the coherent short-period space–time energy release. The resulting images of the discrete coherent-energy distribution (Fig. 3) are qualitatively similar to the initial back-projection images, but differences between the two network images are reduced. Estimates of the rupture velocity using the along-boundary length are in the range 2.0–3.0 km/s (Fig. S5). The total duration of radiation is about 120 s, with the deconvolved images favoring rupture extending to −41°W, about 300 km eastward from the epicenter, somewhat beyond the 250 km extent of the aftershocks (Fig. S1).

We apply the same procedure to the August 4, 2003 earthquake using short-period (0.5–2 s) P recordings from stations in the Americas (Fig. 3(d)), giving the deconvolved distribution of coherent high-frequency radiation locations shown in Fig. 3(c). This image suggests bi-lateral rupture expansion with a total rupture length of ~80–100 km. The rupture velocity is not well constrained, but 2.5 km/s is consistent with the data. Comparison of the images for the 2003 and 2013 events from the Americas network indicates strong overlap between the eastern portion of the 2013 event and the 2003 event (Fig. 3). The westernmost short-period radiation for the 2003 event does lie in the gap between the main high-frequency radiation regions for the 2013 event. The image for the 2013 event extends eastward of the 2003 image, suggesting that the 2013 rupture managed to propagate across the 2003 failure zone. These back-projection images are generally compatible with results in

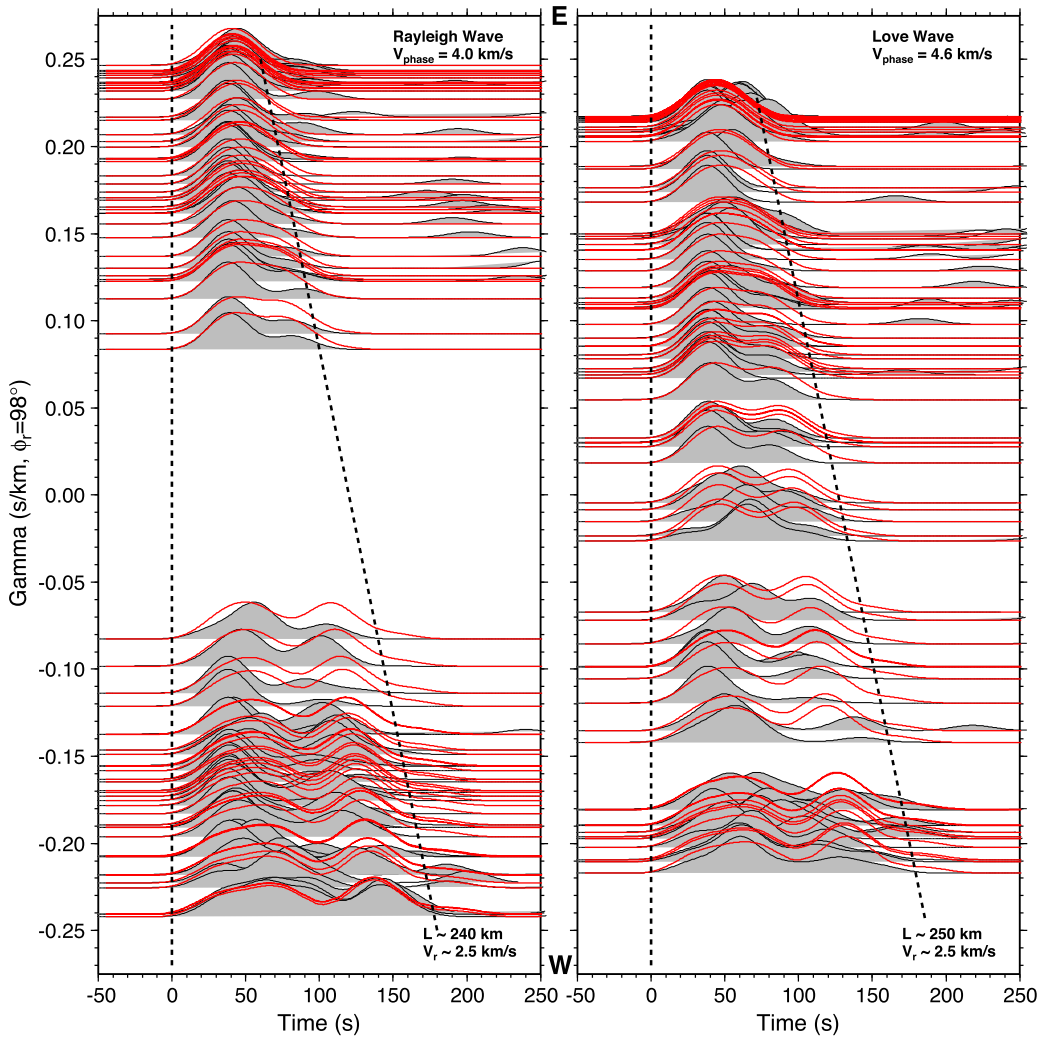

Fig. 4. Effective source time functions (normalized) for R1 Rayleigh waves and G1 Love waves for the November 17, 2013 M_w 7.8 Scotia earthquake, plotted as a function of directivity parameter, gamma $= \cos(\phi - \phi_r)/V_\phi$, for a rupture azimuth ϕ_r of 98° and azimuth of station ϕ, assuming phase velocities V_ϕ of 4.0 km/s (R1) and 4.6 km/s (G1). Each source time function is obtained by deconvolving the group-velocity windowed surface waves by corresponding point-source synthetics from normal model summation using the global Centroid moment tensor source. This removes most propagation effects and allows azimuthal patterns in the source functions to be analyzed for rupture directivity. The red lines are predicted source functions from our preferred finite fault model (Fig. 5(a)) at corresponding azimuths. The black dash lines indicate the estimation of the rupture length and rupture velocity. The source functions narrow toward the east due to the eastward rupture directivity.

Vallée and Satriano (2014) and those posted on the IRIS website (http://www.iris.edu/spud/backprojection). Given the limited resolution of the back-projections, and the uncertain relation between slip and coherent short-period radiation (Lay et al., 2012), we cannot confidently establish whether the 2013 event re-ruptured the large-slip area of the 2003 event using back-projection analysis, but the 2013 rupture certainly at least bracketed the 2003 rupture.

2.3. Surface wave directivity analysis

To provide further constraint on the rupture directivity, we deconvolve global, teleseismic group-velocity-windowed R1 Rayleigh waves and G1 Love waves for the November 17, 2013 M_w 7.8 earthquake by point-source normal-mode synthetic seismograms computed using the gCMT moment tensor for the PREM Earth model, following the method described by Ammon et al. (2006). The resulting propagation-corrected surface wave source time functions (STFs), aligned using the directivity parameter assuming an along-plate boundary rupture azimuth of 98°, show an approximately linear trend for the total durations and two primary intervals of large moment rate (Fig. 4). This supports the strong unilateral eastward rupture expansion. The STF total durations range from about 60–180 s and about 70–180 s for R1 and G1, respectively. The estimated rupture length is ~240–250 km, and the rupture velocity is ~2.5 km/s, assuming a unilateral rupture model and reference phase velocities of 4 km/s for R1 and 4.6 km/s for G1. These results are compatible with the back-projection estimates. The STFs show some variations that suggest non-uniform slip, and provide first-order long period source characteristics that we use to constrain the finite-fault modeling below.

3. Finite-fault modeling

Finite-fault rupture models for the August 4, 2003 and November 17, 2013 South Scotia Ridge earthquakes are obtained by inverting teleseismic broadband P and SH wave ground displacements in the passband 0.005–0.9 Hz (Figs. S6, S7). We use the least-squares kinematic inversion method with positivity constraint for constant rupture expansion velocity (V_r), specified fault geometry, and subfault source time functions parameterized by several overlapping triangles developed by Kikuchi and Kanamori (1991). We modify the code to allow for several fault segments

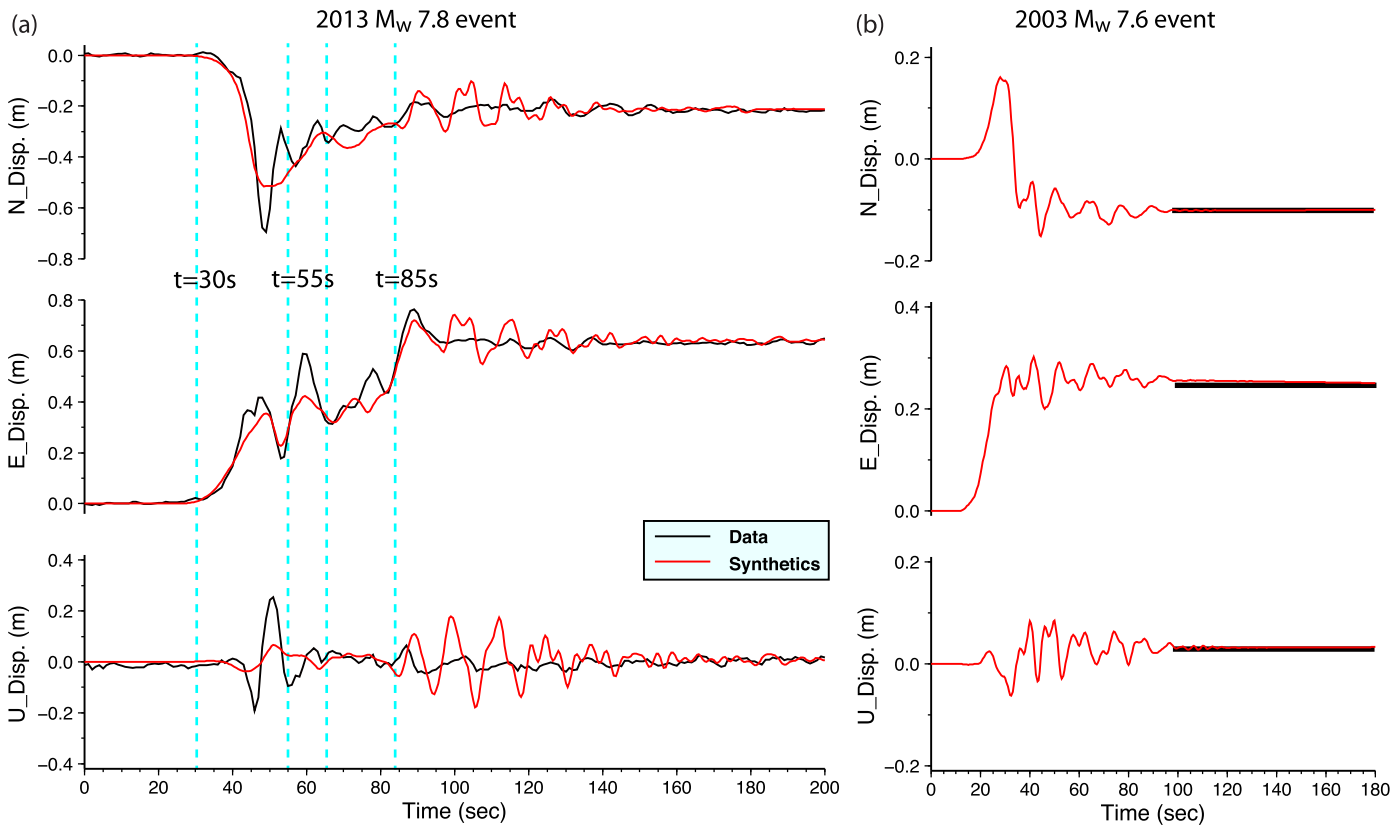

Fig. 5. Forward modeling predictions of 1-Hz sampled GPS ground motion recordings for the November 17, 2013 M_w 7.8 Scotia earthquake (a) and static displacement offsets for the August 4, 2003 M_w 7.6 Scotia earthquake (b) at station BORC on Laurie Island (South Orkney Islands) (Figs. 5, 9). The red curves are the predicted displacement from our preferred finite fault models (Fig. 7).

with different geometries and rupture parameters to explore the complex rupture process of the 2013 event.

In addition to global seismic observations, we model ground motion recordings (Fig. 5) from GPS station BORC on Laurie Island (South Orkney Islands), just south of the SSRT. We first use the GAMIT/GLOBK daily processing to calculate the co-seismic static offsets for both 2003 and 2013 events. To obtain 2013 high-rate GPS ground motions, we calculate the GPS time series relative to each of 6 regional 1-Hz GPS stations (OHIX, PAL2, FALK, AUTF, UNPA and KEPA, Fig. 2) which are held fixed, remove the pre- and post-event averages, scale the final co-seismic displacement for each component by the static offsets from GAMIT/GLOBK processing, and average the kinematic estimates to give the HRGPS recordings shown in Fig. 5(a). After scaling, differences between both the individual and average, and raw and sidereally filtered seismograms, for both the horizontals and verticals, are negligible at the noise level for HRGPS (∼5 mm). The final static offsets are ∼0.63 m east, 0.22 m south, and 0.003 m vertical (Fig. 5(a)). High-rate data are not available from BORC for the 2003 event, but the static offsets are ∼0.25 m east, ∼0.10 m south, and 0.03 m downward, giving a similar ESE overall displacement direction (Fig. 5(b)). The three-component 1-s sampled co-seismic displacements are modeled for the 2013 event; and the static displacement offset is modeled for the 2003 event.

The crustal structure along the SSRT and under the South Orkney micro-continent is not well-known, so we assume a simple two-layer 25-km thick continental crust (Busetti et al., 2000; Vuan et al., 2000) overlain by a thin oceanic layer (1.5 km) for computing Green functions for both teleseismic and regional modeling. Complete ground motions including time-varying and static offsets are computed using a frequency-wavenumber (F-K) integration method (Computer Programs in Seismology, Robert Herrmann) for modeling the BORC recordings. Given that the crustal structure is uncertain, we also perform modeling using regional Green functions for other layered structures, finding that the HRGPS waveforms for the 2013 event are primarily dependent on the space–time rupture history, with only secondary dependence on the precise crustal velocity structure used. Changes in source structure mainly give rise to small variations in seismic moment, as rupture velocity trades-off with local wave velocities for aligning arrivals at BORC.

The BORC static offsets provide valuable constraints on the slip distributions for both events due to the proximity of the station to the ruptures. Fig. 6 indicates initial finite-fault model geometries considered for the 2003 and 2013 events, with the fault planes having the strike and dip of the corresponding gCMT inversions. The grid depicts the centers of subfaults. For assumed uniform slip at each subfault the vectors at the gridpoints indicate the corresponding contribution to the static offset at BORC. These vectors would be weighted by relative slip on each subfault and summed to match the BORC data. If the slip for 2003 were located within the −44.5° to −42° longitude range indicated by back-projection (Fig. 3), it would not be possible to match the BORC displacements which are toward the ESE. The only way to match those offsets is to have rupture extend further to the west, and to have the southerly offsets from the western slip dominate the northerly offsets from the eastern slip. This holds for different choices of dip or strike of the 2003 segment. Similarly, the 2013 event must involve some balance of western and eastern rupture to match the BORC static motions.

Given only the single HRGPS recording for 2013 and only static offsets for 2003, we adopted a strategy of inverting the teleseismic observations for finite-source models with different parameters (V_r, fault strike and dip, subfault source durations), and then

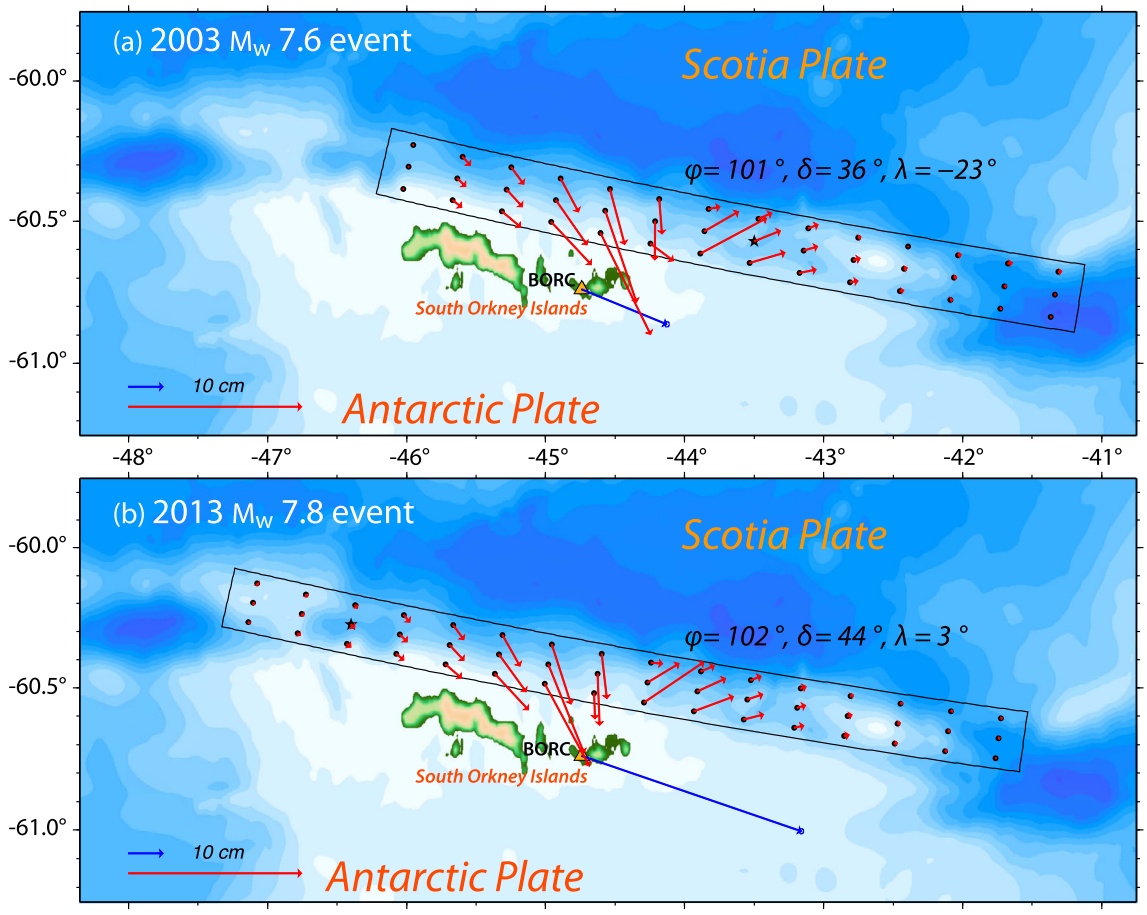

Fig. 6. Initial finite-fault model framework for the 2003 and 2013 earthquakes, with uniform fault models specified by the gCMT best-double couple solutions. The model grids indicate the center of subfaults in the model representations. The GPS station BORC on Laurie Island is indicated, along with the co-seismic static displacement observed for each event, shown with the blue vector. The red vectors indicate the predicted static motion at BORC for a model with uniform slip of 2 m over each fault model with the indicated strike (ϕ), dip (δ) and rake (λ). For the 2003 event (a), the actual slip on the fault must involve significant slip west of longitude −44°, in order to match the ESE motion at BORC, given that the rupture begins to the east (star). For the 2013 event (b), the actual slip on the fault must involve significant slip east of −44° to reduce the southerly motion caused by expected large slip west of −44°.

forward modeling the BORC observations for the resulting models. We then iteratively constrain the choice of faulting parameters used in the finite-source inversions to those matching the salient features of the BORC observations; relative timing and shape of the time-varying displacements and final static offsets (only the latter for the 2003 event). This iterative inversion/modeling procedure yields good constraints on slip distribution along strike, with much better spatial resolution than the teleseismic inversions on their own. The relatively coarse spatial grid appropriate for the teleseismic inversion produces some roughness in the predicted motions for the portion of the fault where rupture moves away from BORC, but the overall character of the signals is modeled reliably.

The body wave inversion model parameterizations are guided by the gCMT best double couple solutions, aftershock sequences, back-projection images, STF observations, and orientation of the plate boundary. The teleseismic data for the 2013 event can largely be reconciled with a single fault orientation throughout the rupture other than for energy after about 110 s, which indicates a change in fault strike on the eastern end of the rupture. In modeling the static offset at BORC for 2003, we found the shallower dip of the gCMT solution provided better fit, so we adopt a two-dip, three-segment model for the 2013 rupture with the western segment having the 45° dip of the gCMT solution for 2013, and the eastern segments having the 36° dip of the gCMT solution for 2003. Dip is not tightly resolved, and has uncertainty of 10° or so, but this choice ensures consistency with the long-period mechanisms on average. The V_r, initial timing, source time function, and geometry for each segment are explored over a large range of parameters, under the constraint of matching the HRGPS recordings. This results in a final model with three fault segments (Fig. 7(a)) with minor changes in strike and dip from west to east. The HRGPS observations are particularly valuable for constraining the timing and geometry of the first two segments, with little constraint on the remote third segment to the east. In order to match the total seismic moment and geodetic measurements we have to use short source time functions for each subfault, comprised of 3 overlapping triangles with rise times of 3.5 s (western segment), 2.0 s (central segment) and 1.5 s (eastern segment), giving maximum subfault rupture durations of 14–6 s. A rupture velocity of 2.5 km/s is used for the preferred model, as indicated by the surface wave STF directivity and short-period back-projection observations. This value is also preferred from a range of choices considered in modeling the HRGPS recordings.

Given the horizontal grid spacing of 22.5 km for the first two segments and the specified rupture velocity, the rupture behaves as a slip-pulse sweeping unilaterally toward the east; longer sliding of initially ruptured subfaults is not compatible with the HRGPS data. There is an initial interval of very weak radiation in the P waves, extending for about 10 s prior to onset of strong arrivals. We delay rupture expansion for the first 4.5 s after the origin time based on lack of any offset from the epicenter in the P wave back-projections. The fits to teleseismic data are not af-

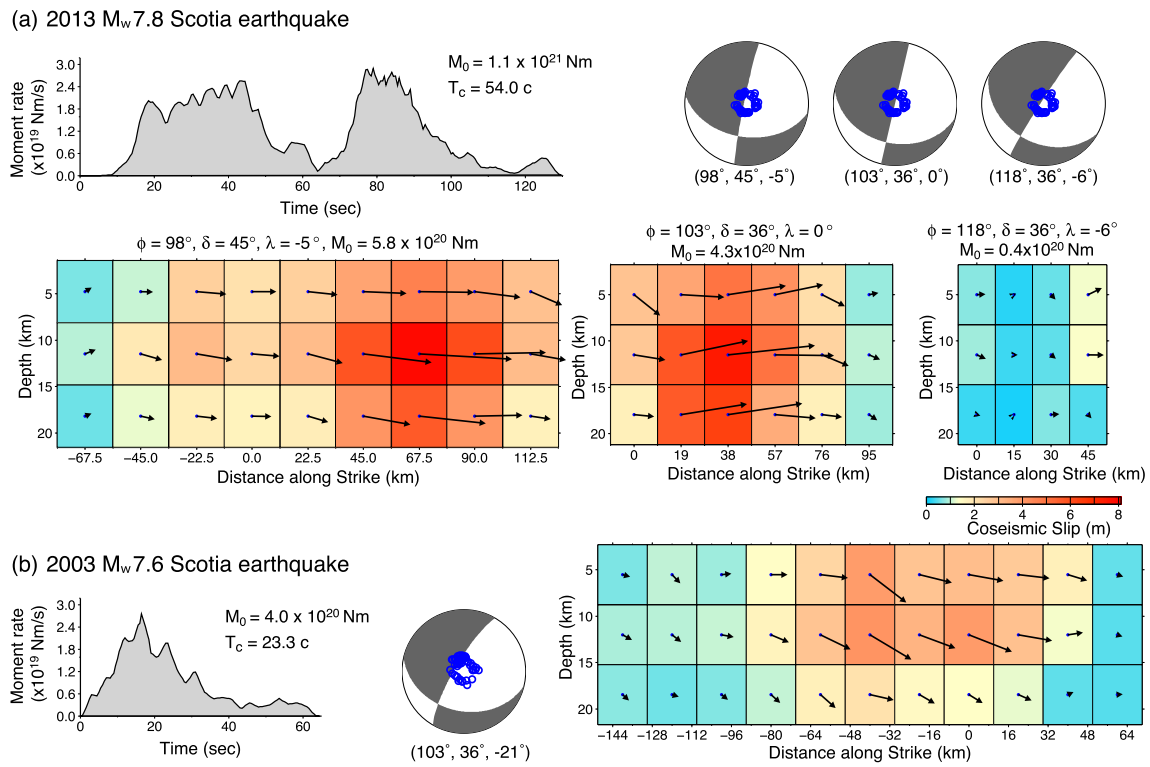

Fig. 7. Finite-fault slip models from inversion of teleseismic body waves (P and SH) for (a) November, 17, 2013, and (b) August 4, 2003 Scotia earthquakes. The slip distribution on the fault plane is shown with the arrows indicating average rake of each subfault, and slip magnitude being color-coded. Three contiguous fault segments with different geometries are used for the 2013 event with relative locations shown in Fig. 9(a). Rupture expansion velocity of 2.5 km/s is used for both events. The moment-rate functions, seismic moments, centroid time shift (T_c) and the average focal mechanism for each fault segment are shown, with lower hemisphere equal area projections indicating the positions sampled by teleseismic P waves used in the inversions. Observed and synthetic waveform comparisons are shown in the supplementary Fig. S6 and Fig. S7.

fected by this, but the HRGPS observations are very sensitive to absolute space–time placement of the slip, and a lower rupture velocity would be required if this delay in rupture expansion were not imposed.

The E–W HRGPS recording for the 2013 event shows two clear steps in the development of the total static offset (Fig. 5(a)). Time-varying motions began about 30 s after the origin time, with initial southward, eastward and downward displacements of 0.7 m, 0.5 m, and 0.2 m, respectively. The rupture begins about 100 km west of the station and sweeps past about 40 km to the north at around 55 s after the origin time. At that time, a second 10-s duration pulse of eastward motion begins with no motion on the N–S and vertical components, followed by about 20 s of minor time-varying motion. At around 85 s, a second eastward step commences, again with minor motions on the N–S and vertical components. The rupture is located well to the east of the station at this time.

The final model for the 2013 event (Fig. 7(a)) has several key attributes. (1) The seismic moment of the first segment (5.8×10^{20} Nm) involves up to ~8 m of slip with a strike of 98° and southward dip of 45°, with rupture extending ~79 km westward and ~124 km eastward from the epicenter. S and Rayleigh waves from near the hypocenter produce the initial large southeastward motions at BORC with slip near the eastern end producing strong eastward Love waves displacements at BORC. (2) The second segment ruptures from ~70–100 s with a seismic moment (4.3×10^{20} Nm) produced by up to 7.5 m of slip with a strike of 103° and southward dip of 36°. This rupture extends ~100 km eastward of the first segment, and produces ENE displacement at BORC that reduces the total southward static motion. The shallower dip of this segment helped to match the total static offset on the N–S GPS record, which is controlled by interference of the contribution from the slip on the first two segments. (3) Minor seismic moment (0.4×10^{20} Nm) is found on the easternmost segment with strike 118° and southward dip of 36°, from modeling late (110–120 s after origin) P wave signals in the azimuthal range of 100°–200° (observed and final model waveform comparisons are shown in Fig. S6). (4) The two large moment rate pulses are compatible with the high-frequency coherent bursts from the back-projections both temporally and spatially. Forward prediction of the surface wave STFs for this model generally matches the directivity and two-pulse character of the data, as seen in Fig. 4. (5) The average slip on the first segment is ~3.4 m and the average stress drop is 3.9 MPa, with the corresponding values for the second segment being ~4.0 m and ~5.8 MPa, with these being computed for the subfaults with moment larger than 15% of the peak subfault moment. The total moment of the finite fault inversion with constraint from modeling the GPS recording at BORC is $\sim 1.1 \times 10^{21}$ Nm, which is ~89% higher than the moment from long-period point source inversion. This discrepancy may be due to differences in precise fault geometry as well as uncertainty in the absolute location of the fault model relative to the GPS station.

The lack of clear directivity yields fewer constraints on the finite-fault inversion for the 2003 event. The ESE static offset at BORC indicates that the main slip during the 2003 event must be different from the slip in the second segment of the 2013 event, which produced ENE contributions to the total BORC displacement for that event (Fig. 6). This proves to be a very influential observation for constructing our preferred model; if we adopt the gCMT focal mechanism and allow a bilateral rupture from the 2003 hypocenter, we cannot match the BORC observation although the fit to teleseismic P and SH data is acceptable. By iteratively performing inversions of the seismic data with varying fault orientations, rupture velocity and lateral fault extent and

then predicting the BORC static offsets for the resulting models, we established that the main slip during the 2003 event must locate relatively close to BORC, westward of the hypocenter, with a shallow dipping fault (we obtain good fits using the 36° dip of the gCMT solution). The preferred model gives a good fit to teleseismic body waves (Fig. S7) and satisfactory match of the GPS offsets (Fig. 5(b)), for a fault geometry with strike 103° and southward dip of 36° (Fig. 7(b)). This geometry is the same as for the second segment in the 2013 model, thus it is plausibly the same fault surface that ruptured, but the peak slip in 2003 locates further west than in 2013. The seismic moment is 4.0×10^{20} Nm, the total duration is ~60 s, the average slip is 2.2 m, and average stress drop is 2.5 MPa. The slip and stress drop are similar to the values for the two main segments in the 2013 event. The contributions to the static offsets at BORC for the subfaults in the final finite-fault models are shown in Fig. S8. The large-slip region in the 2003 model thus locates in the region of low slip between the two patches that ruptured in 2013 (see Fig. S9), and this is strongly constrained by the ESE static offset observed at BORC.

4. Radiated seismic energy

Slip-pulse rupture processes are indicated for the 2003 and 2013 strike-slip events, with rise-times less than 14 s, much shorter than the total durations of the sources. We calculated the azimuthally-averaged far-field source spectra and seismic moment-scaled radiated energy (E_R/M_0) for both events. The average broadband source spectra (Fig. 8) were obtained by combining the spectra of the moment-rate functions for the preferred finite-fault models in Fig. 7 for frequencies less than ~0.05 Hz with averaged P wave spectra for frequencies from 0.05–1.5 Hz. Average radiated energy from individual P wave spectra was estimated following the procedure of Venkataraman and Kanamori (2004), and then the energy distribution across the entire spectrum was scaled up based on the composite spectra in Fig. 8. Most of the energy is from frequencies >0.05 Hz. For the 2003 event, the radiated energy is 9.1×10^{15} J, and for the 2013 event it is 1.4×10^{16} J. There is at least a factor of two uncertainty in radiated energy estimates, but these values can be compared with those reported in Lay et al. (2012), which were determined by the same procedure. The source spectrum for the 2003 event is similar to the reference ω-squared source spectrum with 3 MPa stress parameter, whereas the source spectrum for the 2013 event is somewhat depleted in high-frequency (>0.5 Hz) radiation. The individual station estimates of P wave radiated energy for the 2013 event show strong azimuthal variation (Fig. S10), as expected given the ~250 km long unilateral rupture. The seismic moment-scaled radiated energy (E_R/M_0) is $\sim 3.3 \times 10^{-5}$ for the 2003 event and $\sim 2.5 \times 10^{-5}$ for the 2013 event, using the gCMT M_0 values. These ratios are comparable to values for intraplate earthquakes (Lay et al., 2012). The relatively high moment-scaled energy values may be associated with the shallow-dipping strike-slip geometry on which there is not large lateral offset.

5. Discussion

The finite-fault slip distributions for the 2003 and 2013 events are shown in map view in Fig. 9, along with their foreshock and aftershock sequences. The GPS static motions and model predictions at station BORC are also shown, illustrating the sensitive location of the station to the two slip distributions. The M_w 7.6 2003 event (Fig. 9(a)) appears to have some bilateral character, compatible with the aftershocks and back-projection images, but the primary large slip region is concentrated to the west of the epicenter, NNE of BORC, based on the ESE static motion at that station. The shallow dipping rupture plane is consistent with the gCMT solution,

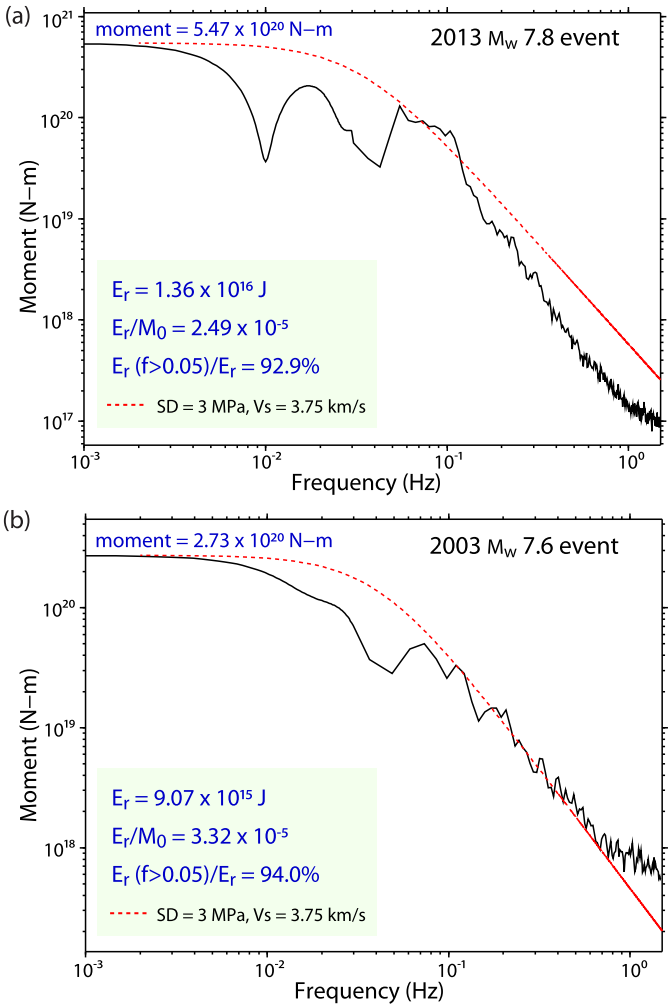

Fig. 8. The average source spectra for (a) November 17, 2013 M_w 7.8 Scotia earthquake, and (b) August 4, 2003 M_w 7.6 Scotia earthquake. The black lines indicate the observed spectra, estimated at frequencies less than ~0.05 Hz from the moment-rate functions inverted from teleseismic body wave observations (Fig. 7) scaled to gCMT seismic moment values, and at frequencies >~0.05 Hz from stacking of broadband teleseismic P wave spectra. The dashed red lines are reference source spectra for an ω^{-2} model with 3 MPa stress parameter, shear velocity 3.75 km/s, and seismic moments from gCMT solutions. The radiated energy over the full frequency band, E_r, is estimated based on average source spectra and the average radiated energy from 0.05 to 1.5 Hz from teleseismic P waves (see supplementary Fig. S10). The high seismic moment scaled radiated energy, $\sim 2.5–3.3 \times 10^{-5}$, is similar to the level for intraplate earthquakes near subduction zones (Lay et al., 2012).

and the sinistral motion parallels the relative motion of the plates closely. The M_w 7.8 2013 earthquake sequence initiated with two left-lateral strike-slip foreshocks with magnitudes M_w 6.1 (November 13) and M_w 6.8 (November 16), located up to ~50 km west of the mainshock. Aftershocks of the mainshock extend ~250 km eastward along the SSRT, extending across the 2003 slip zone and aftershock area. There is minor change in geometry along strike with shallower dip in the eastern segments, but aftershocks tend to cluster around the large slip regions of the 2013 event. The large slip zone for the 2003 event thus lies in between the two main slip patches of the 2013 event, suggesting that while the aftershock zones may overlap, the peak slip patterns are largely complementary and this is not a simple re-rupture of a previously slipped region just ten years later as has been suggested by Vallée and Satriano (2014). The finite-fault models do have overlapping slip in the 2003 rupture area with lower slip, so some re-rupture cannot be excluded, but the peak slip is largely complementary (Figs. 9

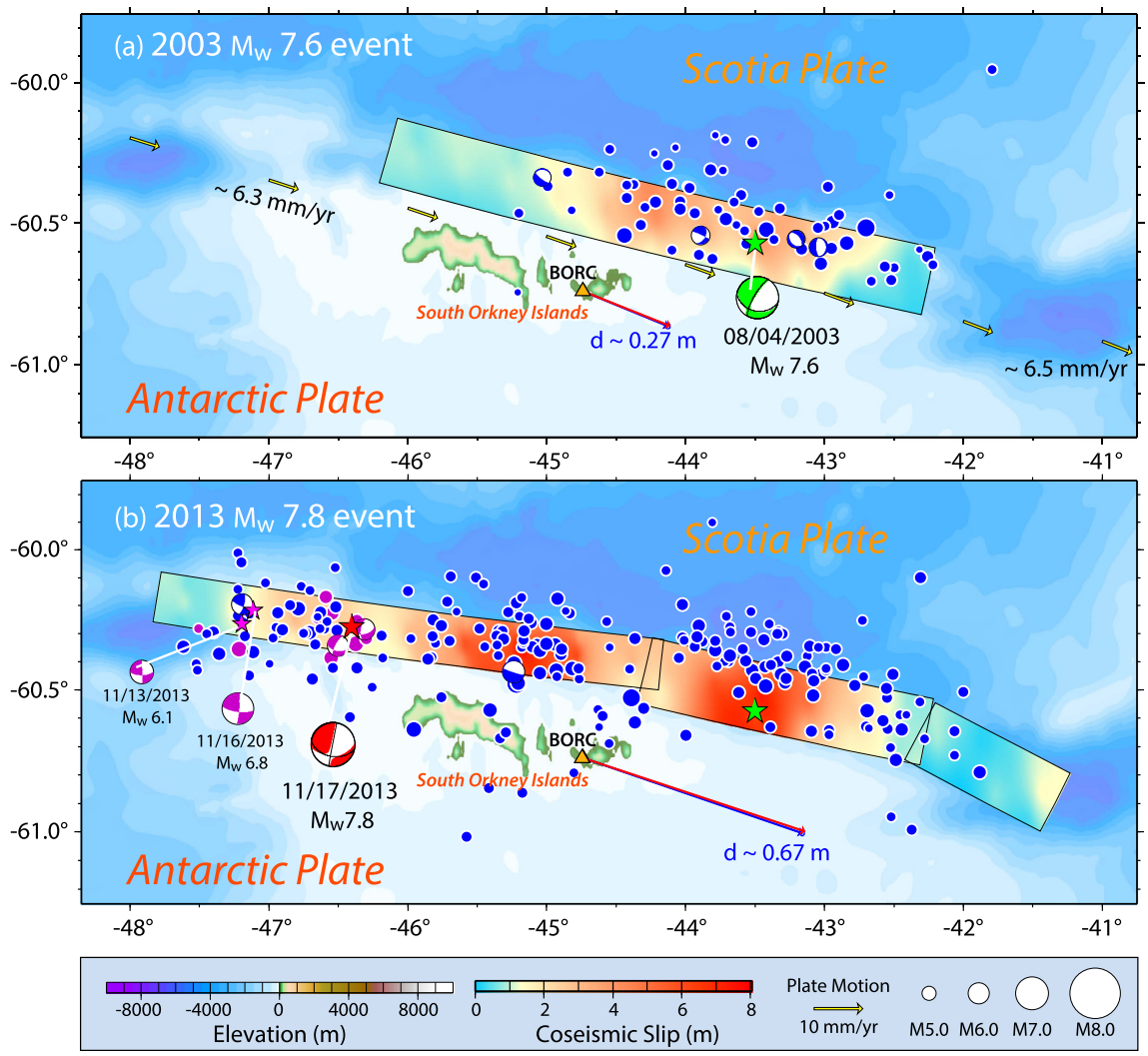

Fig. 9. Map display of our preferred fault slip models (Fig. 7), and foreshock (purple circles) and aftershock sequences (blue circles) for August 4, 2003 M_w 7.6 (a) and November 17, 2013 M_w 7.8 (b) events. Focal mechanisms are global Centroid Moment Tensor (gCMT) solutions. Yellow arrows in (a) indicate the plate motion direction and rate along the plate boundary between the Scotia plate and Antarctica plate, relative to the fixed Scotia plate from model MORVEL (DeMets et al., 2010). The observed (blue) and predicted (red) static ground motions at GPS site BORC are shown with arrows.

and S9). Modeling the GPS data at BORC is critical for coming to this conclusion.

The 2003 peak slip area may have been delimited between two strongly coupled zones (asperities) that subsequently ruptured in 2013. The latter event may have re-ruptured continuously through the 2003 peak slip zone with low displacement, or the easternmost region may have been dynamically triggered in 2013 by strong shear waves from the western asperity. Our slip models do not have the resolution to establish that there was no slip between the two 2013 asperities. Given the strong eastward directivity of seismic wave radiation evident in the GPS recording at BORC for the western portion of the 2013 rupture, either seismic release of residual or newly accumulated stress in the 2003 zone or jumping of slip across that zone may have occurred.

Dynamic triggering is a possible factor in the occurrence of the November 25, 2013 (06:27:33 UTC, 53.945°S, 55.003°W) M_w 7.0 event on the NSRT (Fig. 1), which was preceded by magnitude 5.4 and 5.6 earthquakes on November 24, 2013. Examination of broadband recording at station EFI [East Falkland Island (Malvinas)] for the November 17 mainshock could not establish whether any small events were immediately activated in the vicinity of the November 25, 2013 event along the NSRT, though they could have been obscured by observed prolonged T-phase arrivals from the mainshock. The relatively low rate of seismicity along the NSRT suggests that this event was triggered (time advanced). Calculation of the November 17, 2013 Rayleigh wave amplitude at the location of November 25 event indicates that the dynamic strain was about 2×10^{-7}, which is near the threshold for statistically significant levels of dynamic triggering.

These large South Scotia Ridge events are located at the northern margin of the South Orkney micro-continent, spanning longitudes from ~48°W to 42°W. This continental fragment has ~25 km thick crust based on gravity modeling. To the north lies an east–west trending depression called the South Orkney trough (Busetti et al., 2000; Civile et al., 2012; Vuan et al., 2000) along which the main slip patches in the 2003 and 2013 events are located. While the current plate motions are largely left-lateral shear along this ~350 km long east–west segment, a minor convergent component, involving underthrusting of the Scotia plate below the Antarctic Plate is suggested by presence in the west of an accretionary prism. This accretionary prism is manifested in a smooth step morphology, by abrupt change in the seismic characteristics at the outer deformation front, and by continent-

ward dipping reflectors in seismic profile (Busetti et al., 2000; Civile et al., 2012; Kavoun and Vinnikovskaya, 1994; Lodolo et al., 2010; Maldonado et al., 1998). This region is distinct from the western SSRT, the Bransfield basin, which appears to be related to back-arc spreading associated with subduction along the South Shetlands Trench (Fig. 1); and from the eastern SSRT along the boundary of the Brune deep and extending to the Discovery Bank which may be associated with the subduction of the Weddell Sea under the Scotia plate. Earthquake mechanisms along the SSRT include normal fault solutions in small pull-apart basins and some oblique motions, but the purely sinistral motion of the two largest events in the region in 2003 and 2013 indicates that this is the dominant strain release process operating along the central SSRT.

Both the 2003 M_w 7.6 and 2013 M_w 7.8 events have predominantly strike-slip motion on shallow-dipping faults, whereas strike-slip transform faults are typically steeply dipping, as that is energetically more favored. We infer that the fault planes are inherited underthrusting fault geometries from past convergence. The SSRT is predominantly transtensional at present, with restraining and releasing bend structures. The thrust faults along the South Orkney micro-continent are likely to be relic structures from continental break-up that transported to their current configuration. It is not clear how the primarily sinistral relative motion developed, but the current rate of deformation and total offsets on the faults are modest, and one explanation is that the change in plate motion along the SSRT occurred rapidly enough that slip partitioning did not lead to development of an upper plate vertical strike-slip fault. This has some similarity to the September 24, 2013 M_w 7.6 Pakistan earthquake, which has a purely strike-slip motion on a 45° dipping fault plane that likely originally formed as a thrust fault within the Makran accretionary prism, activated by subsequent left-lateral shear along the Chaman fault system due to India colliding with Eurasia to the east (Avouac et al., 2014). For the slow relative plate rate of ~6–7 mm/yr of sinistral motion along the SSRT (DeMets et al., 2010; Smalley et al., 2007), the recurrence time for the 2003 and 2013 earthquakes with peak slip of ~8 m and average slip of ~4 m, is estimated to be ~600–1300 yrs.

6. Conclusions

The 2003 M_w 7.6 and 2013 M_w 7.8 South Scotia Ridge earthquakes ruptured the plate boundary along the South Orkney micro-continent with the sinistral strike-slip motion on a ~36–45° shallow-dipping fault plate. Using constraints on the faulting geometry and rupture velocity provided by long-period surface wave source time functions and short-period P wave back-projection images, a finite-fault solution for the 2013 event is obtained by iterative inversion of broadband P and SH waves and forward modeling of 1-Hz HRGPS recordings at station BORC, located near the middle of the rupture. The main slip areas for the 2013 event bracket the main slip area for the 2003 event inferred from inverting teleseismic body waves and modeling the static offset at BORC. Thus, the 2013 event appears to have ruptured or triggered across the 2003 zone, yielding largely complementary large slip regions that combine to give relatively uniform slip along the fault strike. The almost purely strike-slip motion of the 2003 and 2013 events may be associated with reactivation of an inherited thrust fault that originally formed from compression across the boundary during continental fragmentation or possibly seafloor spreading of the Scotia plate as it developed its current configuration.

Acknowledgements

This work made use of GMT and SAC software. The IRIS DMS data center was used to access the seismic data from Global seismic network and Federation of Digital Seismic Network stations. We thank the Argentine National Park Service and Argentine Navy for operation of BORC. We thank R. Abercrombie and an anonymous reviewer for their helpful reviews of the manuscript. This work was supported by NSF grant EAR1245717 (T.L.).

Appendix A. Supplementary material

Supplementary material related to this article can be found online at http://dx.doi.org/10.1016/j.epsl.2014.06.007.

References

Allen, T.I., Marano, K.D., Earle, P.S., Wald, D.J., 2009. PAGER-CAT: a composite earthquake catalog for calibrating global fatality models. Seismol. Res. Lett. 80 (1), 57–62. http://dx.doi.org/10.1785/gssrl.80.1.57.

Ammon, C.J., Velasco, A.A., Lay, T., 2006. Rapid determination of first-order rupture characteristics for large earthquakes using surface waves: the 2004 Sumatra–Andaman earthquake. Geophys. Res. Lett. 33, L14314. http://dx.doi.org/10.1029/2006GL026303.

Avouac, J.P., Ayoub, F., Wei, S., Ampuero, J.P., Meng, L., Leprince, S., Helmberger, D., 2014. The 2013, M_w 7.7 Balochistan earthquake, energetic strike-slip reactivation of a thrust fault. Earth Planet. Sci. Lett. 391, 128–134.

Busetti, M., Zanolla, M., Marchetti, A., 2000. Geological structure of the South Orkney microcontinent. Terra Antarctica 8 (2), 1–8.

Civile, D., Lodolo, E., Vuan, A., Loreto, M.F., 2012. Tectonics of the Scotia–Antarctica plate boundary constrained from seismic and seismological data. Tectonophysics 550, 17–34.

Dalziel, I.W., Lawver, L.A., Norton, I.O., Gahagan, L.M., 2013. The Scotia Arc: genesis, evolution, global significance. Annu. Rev. Earth Planet. Sci. 41, 767–793.

DeMets, C., Gordon, R.G., Argus, D.F., 2010. Geologically current plate motions. Geophys. J. Int. 181, 1–80. http://dx.doi.org/10.1111/j.1365-246X.2009.04491.x.

Forsyth, D.W., 1975. Fault plane solutions and tectonics of the South Atlantic and Scotia Sea. J. Geophys. Res. 80 (11), 1429–1443. http://dx.doi.org/10.1029/JB080i011p01429.

Kavoun, M., Vinnikovskaya, O., 1994. Seismic stratigraphy and tectonics of the northwestern Weddell Sea (Antarctica) inferred from marine geophysical surveys. Tectonophysics 240 (1), 299–341.

Kikuchi, M., Kanamori, H., 1991. Inversion of complex body waves—III. Bull. Seismol. Soc. Am. 81 (6), 2335–2350.

Lay, T., Kanamori, H., Ammon, C.J., Hutko, A.R., Furlong, K., Rivera, L., 2009. The 2006–2007 Kuril Islands great earthquake sequence. J. Geophys. Res. 114, B113208. http://dx.doi.org/10.1029/2008JB006280.

Lay, T., Kanamori, H., Ammon, C.J., Koper, K.D., Hutko, A.R., Ye, L., Yue, H., Rushing, T.M., 2012. Depth-varying rupture properties of subduction zone megathrust faults. J. Geophys. Res. 117, B04311. http://dx.doi.org/10.1029/2011JB009133.

Livermore, R., Balanyá, J.C., Maldonado, A., Martínez, J.M., Rodríguez-Fernández, J., de Galdeano, C.S., Zaldívar, J.G., Jabaloy, A., Barnolas, A., Somoza, L., Hernández-Molina, J., Suriñach, E., Viseras, C., 2000. Autopsy on a dead spreading center: the Phoenix Ridge, Drake Passage, Antarctica. Geology 28 (7), 607–610.

Livermore, R.A., McAdoo, D., Marks, K., 1994. Scotia Sea tectonics from high-resolution satellite gravity. Earth Planet. Sci. Lett. 123 (1), 255–268.

Lodolo, E., Civile, D., Vuan, A., Tassone, A., Geletti, R., 2010. The Scotia–Antarctica plate boundary from 35°W to 45°W. Earth Planet. Sci. Lett. 293 (1), 200–215.

Maldonado, A., Zitellini, N., Leitchenkov, G., Balanyá, J.C., Coren, F., Galindo-Zaldívar, J., Lodolo, E., Jabaloy, A., Zanolla, C., Rodríguez-Fernández, J., Vinnikovskaya, O., 1998. Small ocean basin development along the Scotia–Antarctica plate boundary and in the northern Weddell Sea. Tectonophysics 296 (3), 371–402.

Martos, Y.M., Galindo-Zaldívar, J., Catalán, M., Bohoyo, F., Maldonado, A., 2014. Asthenospheric Pacific–Atlantic flow barriers and the West Scotia Ridge extinction. Geophys. Res. Lett. 41, 43–49. http://dx.doi.org/10.1002/2013GL058885.

Okal, E.A., Hartnady, C.J., 2009. The South Sandwich Islands earthquake of 27 June 1929: seismological study and inference on tsunami risk for the South Atlantic. S. Afr. J. Geol. 112 (3–4), 359–370.

Pelayo, A.M., Wiens, D.A., 1989. Seismotectonics and relative plate motions in the Scotia Sea region. J. Geophys. Res. 94 (B6), 7293–7320. http://dx.doi.org/10.1029/JB094iB06p07293.

Smalley Jr., R., Dalziel, I.W.D., Bevis, M.G., Kendrick, E., Stamps, D.S., King, E.C., Taylor, F.W., Lauría, E., Zakrajsek, A., Parra, H., 2007. Scotia arc kinematics from GPS geodesy. Geophys. Res. Lett. 34, L21308. http://dx.doi.org/10.1029/2007GL031699.

Thomas, C., Livermore, R., Pollitz, F., 2003. Motion of the Scotia Sea plates. Geophys. J. Int. 155, 789–804. http://dx.doi.org/10.1111/j.1365-246X.2003.02069.x.

Vallée, M., Satriano, C., 2014. Ten-year recurrence time between two major earthquakes affecting the same fault segment. Geophys. Res. Lett. 41, 2312–2318. http://dx.doi.org/10.1002/2014GL059465.

Venkataraman, A., Kanamori, H., 2004. Effect of directivity on estimates of radiated seismic energy. J. Geophys. Res. 109 (B4), B04301. http://dx.doi.org/10.1029/2003JB002548.

Vuan, A., Russi, M., Panza, G.F., 2000. Group velocity tomography in the subantarctic Scotia Sea region. Pure Appl. Geophys. 157 (9), 1337–1357.

Xu, Y., Koper, K.D., Sufri, O., Zhu, L., Hutko, A.R., 2009. Rupture imaging of the M_w 7.9 12 May 2008 Wenchuan earthquake from back projection of teleseismic *P* waves. Geochem. Geophys. Geosyst. 10 (Q04006). http://dx.doi.org/10.1029/2008GC002335.

Complementary slip distributions of the August 4, 2003 M_w 7.6 and November 17, 2013 M_w 7.8 South Scotia Ridge earthquakes

Lingling Ye[a], Thorne Lay[a,*], Keith D. Koper[b], Robert Smalley, Jr.[c], Luis Rivera[d], Michael G. Bevis[e], Andrés F. Zakrajsek[f], and Felix Norman Teferle[g]

[a] Department of Earth and Planetary Sciences, University of California Santa Cruz, Santa Cruz, CA 95064, USA
[b] Department of Geology and Geophysics, University of Utah, Salt Lake City, UT 84112, USA
[c] Center for Earthquake Research and Information, The University of Memphis, Memphis, TN 38152, USA
[d] Institut de Physique du Globe de Strasbourg, Université de Strasbourg/CNRS, Strasbourg, France
[e] School of Earth Sciences, Ohio State University, 275 Mendenhall Laboratory, Columbus, Ohio 43210, USA
[f] Ciencias de la Tierra, Dirección Nacional del Antártico - Instituto Antártico Argentino, Argentina
[g] Geophysics Laboratory, University of Luxembourg, Luxembourg, L-1359

[*] Corresponding author. Tel.: +831 459 3164
E-mail address: tlay@ucsc.edu (T. Lay).

Supplementary Information: Figures S1-S10, Animations S1, S2

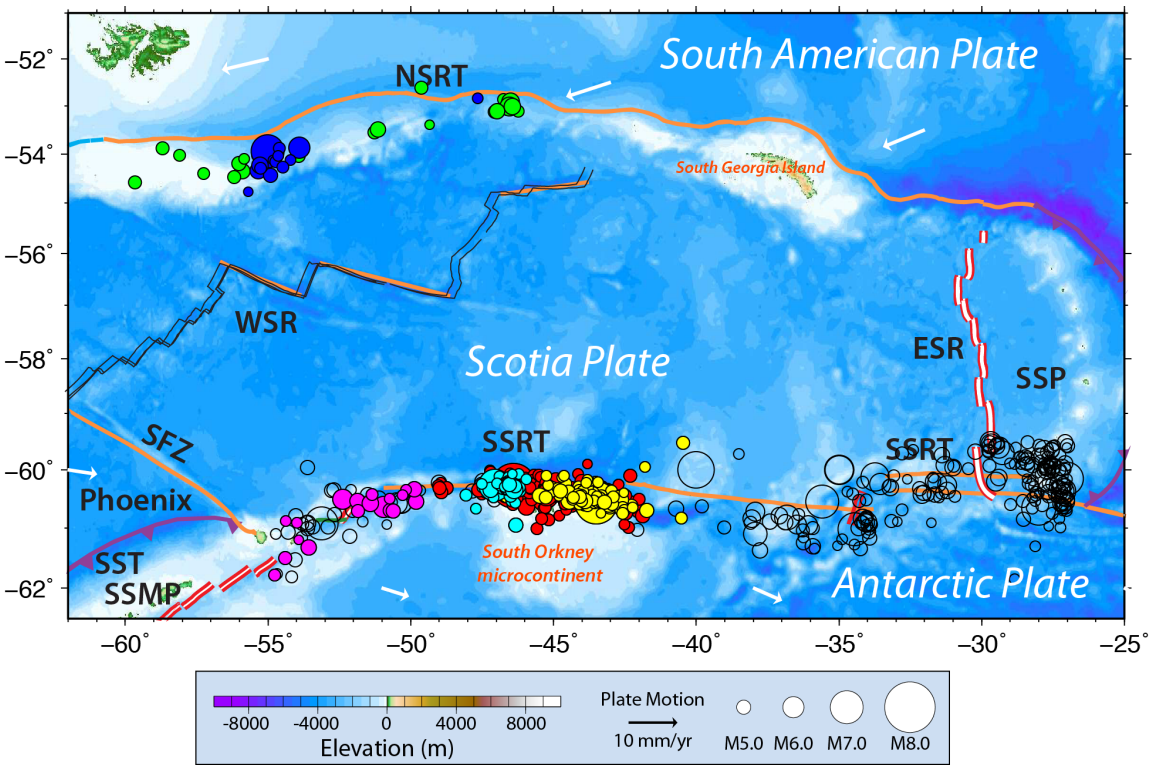

Fig. S1. Seismicity around the Scotia Plate. The black circles indicate epicenters of M ≥ 4.0 events from 1900 to 1975 from PAGER-CAT (Allen *et al.*, 2009) and USGS/NEIC catalog from 1976 to 2014 along the South Scotia Ridge plate boundary between the Scotia plate and Antarctica plate. The color-coded circles show the epicenters of M ≥ 4.0 events commencing with the August 4, 2003 M_w 7.6 event following the time line shown in Fig. S2. Yellow symbols are local aftershocks of 2003, green symbols are activity along the North Scotia Ridge up until the 2013 mainshock, magenta symbols are events west of the 2013 rupture from 2003-2013, cyan symbols are the 2013 foreshock sequence, red symbols are the 2013 aftershocks, blue symbols are the 2013 activity along the North Scotia Ridge transform including the November 25, 2013 M_w 7.0 event. Arrows indicate the plate motion directions and rates relative to a fixed Scotia plate computed using model MORVEL (DeMets *et al.*, 2010). Other symbols are same as Fig. 1.

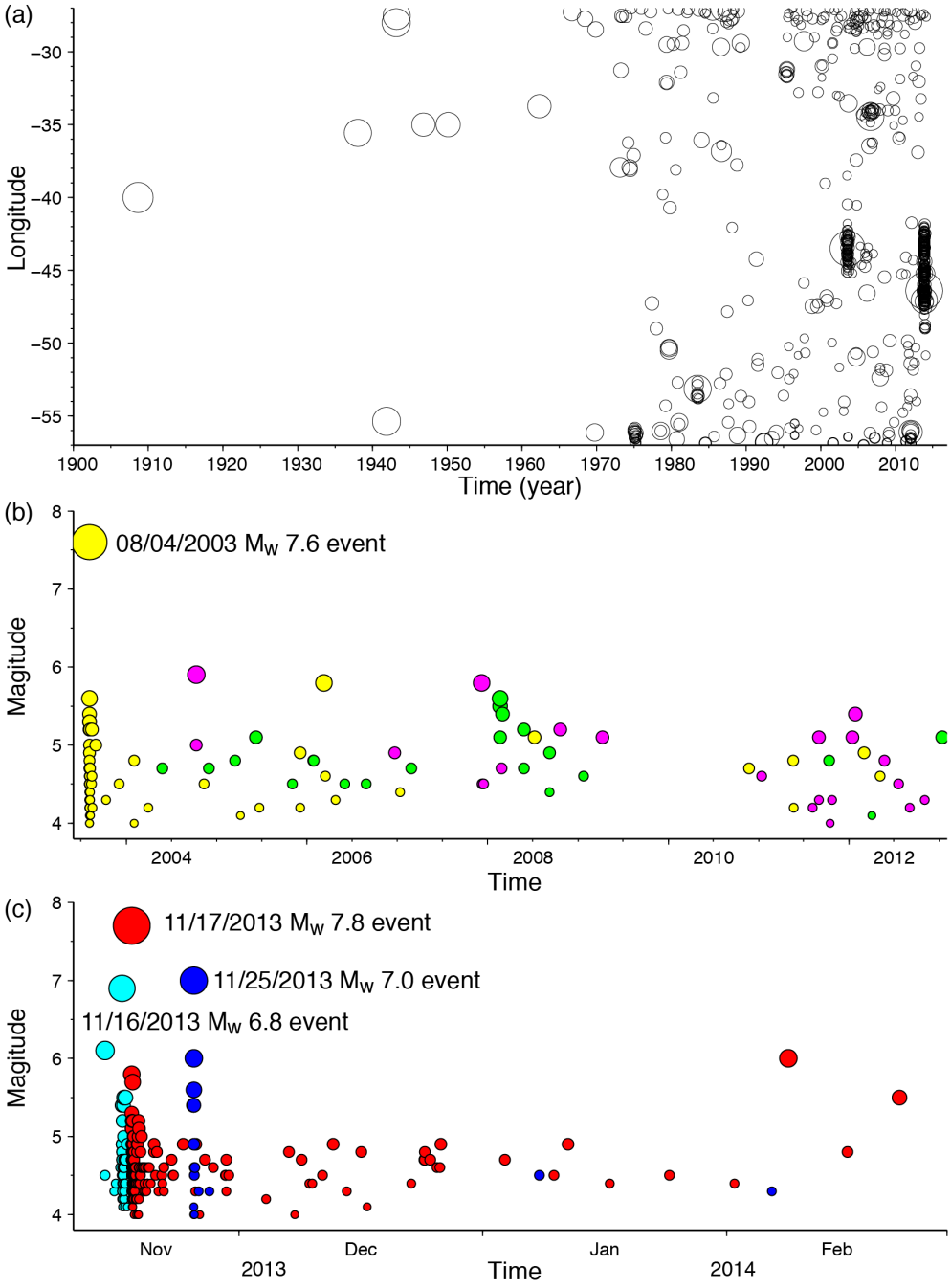

Fig. S2. Time series for the seismicity color-coded as Fig. S1: (a) M ≥ 4.0 events along the South Scotia Ridge plate boundary between the Scotia plate and Antarctic plate; (b) seismicity from the August 4, 2003 M_w 7.6 event to November 2013; and (c) the foreshock and aftershock sequences for November 17, 2013 M_w 7.8 event.

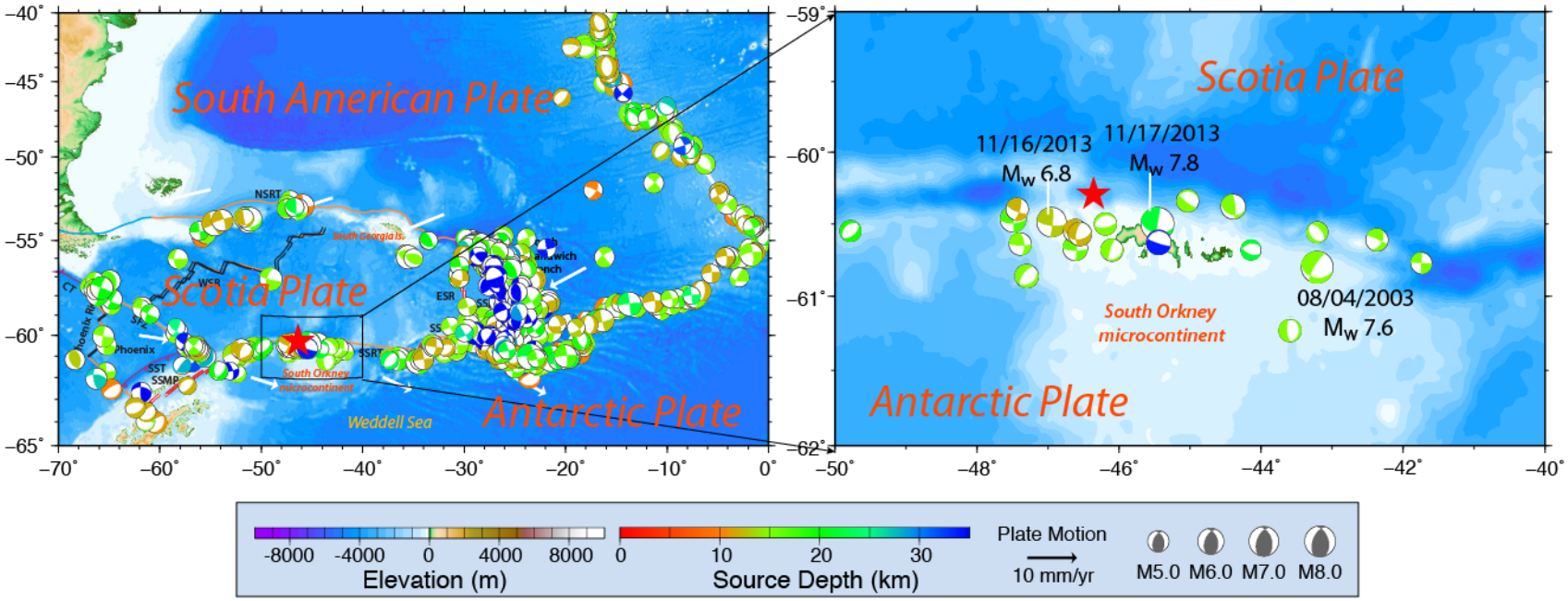

Fig. S3. Maps of gCMT focal mechanisms from 1976 to 2014 for earthquakes around the Scotia Sea plate on regional scale (left) and zoomed in on the region around the 2013 event (right). The red star indicates the epicenter for the November 17, 2013 M_w 7.8 event from USGS/NEIC catalog. Other symbols are same as Fig. 1.

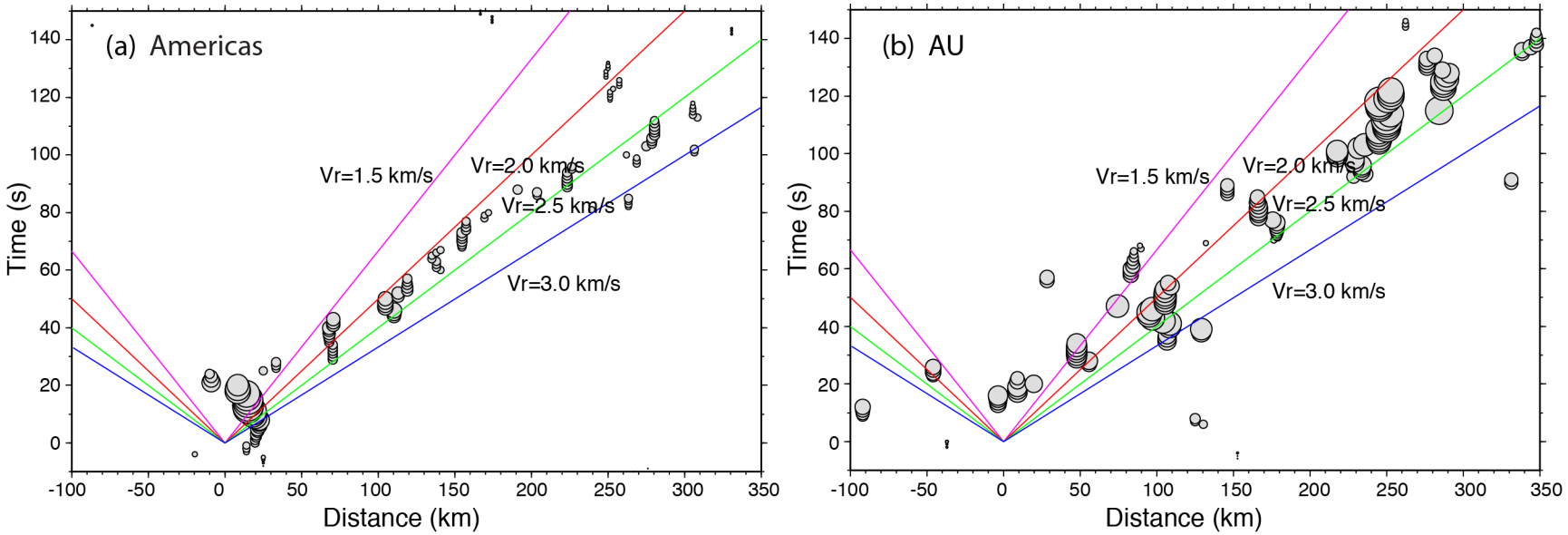

Fig. S4. The space-time sequence of coherent high frequency seismic radiation from the November 17, 2013 M_w 7.8 Scotia earthquake from P wave back-projection (Fig. 2), plotted as distance from the epicenter with positive values eastward. The color-coded lines indicate the slope of different average rupture velocities. A rupture velocity of ~2.0- 2.5 km/s is estimated for back-projections of both Americas and Australia (AU) networks.

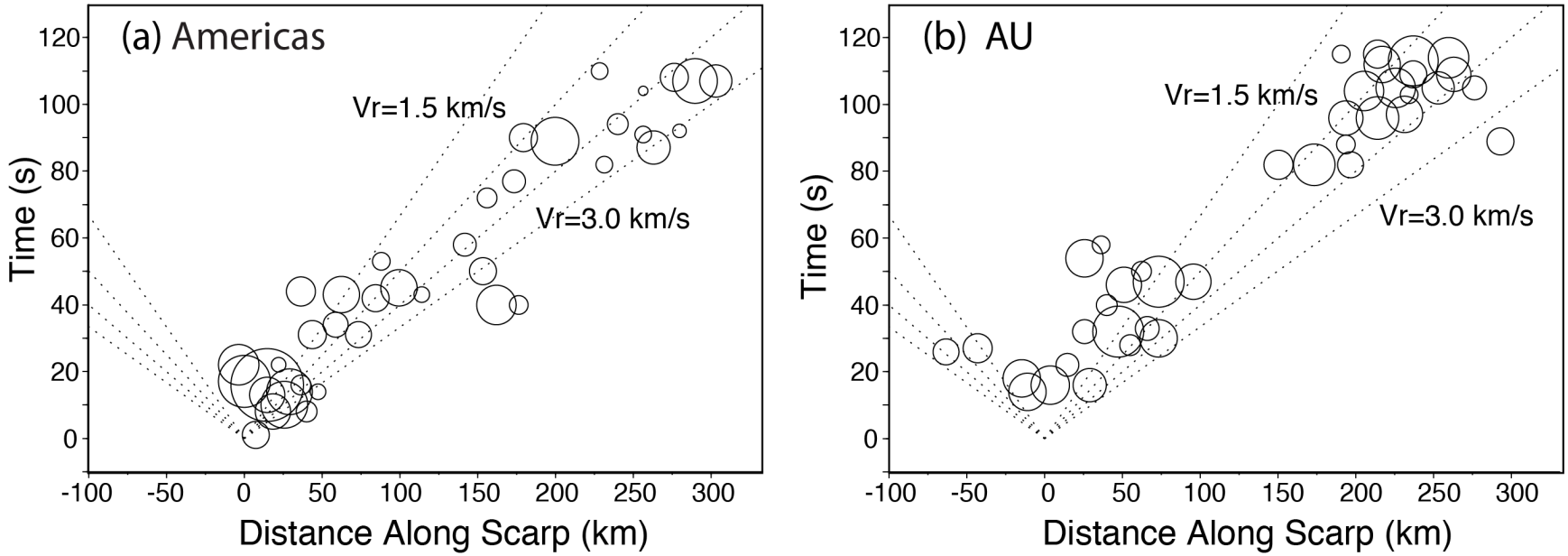

Fig. S5. The space-time sequence of coherent high frequency seismic radiation from the November 17, 2013 M_w 7.8 Scotia earthquake obtained by deconvolving array response functions at 1Hz (Fig. 3), plotted as distance along the plate boundary with positive values eastward. The dashed lines indicate slopes for different rupture velocities. A rupture velocity of ~2.0- 3.0 km/s is estimated for both Americas and Australia (AU) networks.

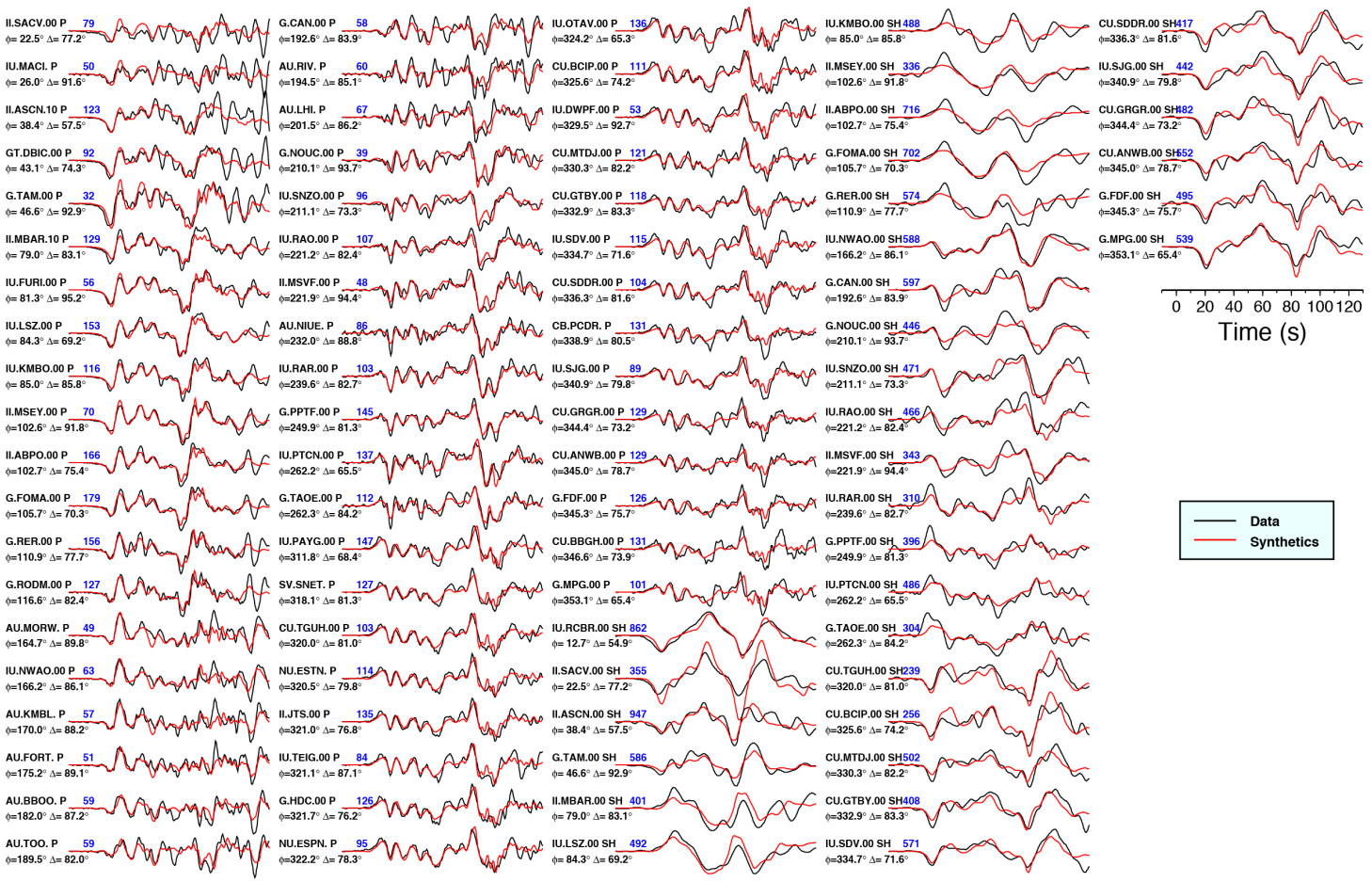

Fig. S6. Comparison of observed (black lines) and modeled (red lines) teleseismic body waves for the November 17, 2013 M_w 7.8 Scotia earthquake. The model shown in Fig. 7a is used for the computations. The signals are broadband ground displacements in the passband 0.005-0.9 Hz. The data and synthetics are normalized by the peak-to-peak amplitude, blue number in unit of 10^{-6} m.

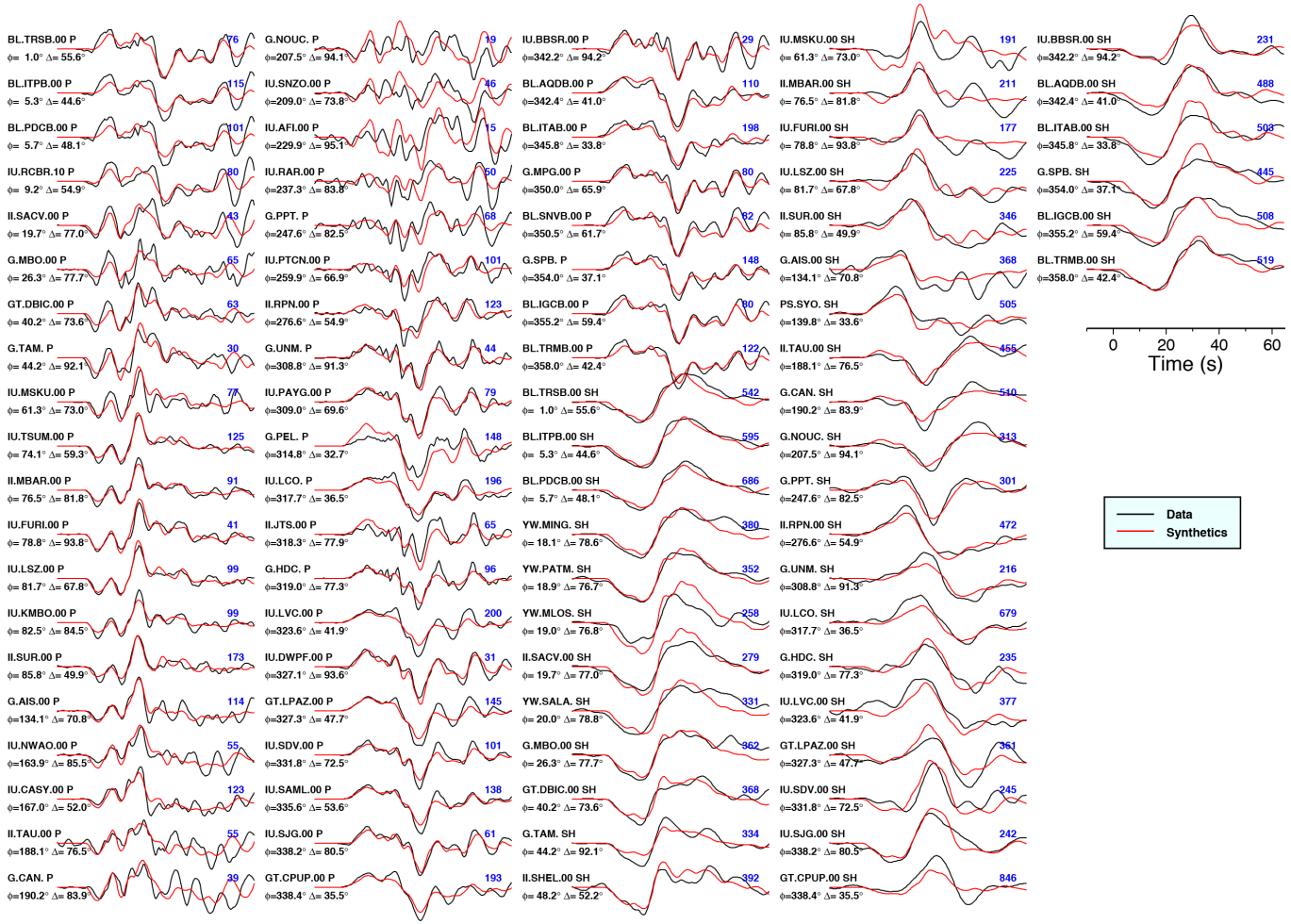

Fig. S7. Comparison of observed (black lines) and modeled (red lines) teleseismic body waves for the August 4, 2003 M_w 7.6 Scotia earthquake. The model shown in Fig. 7b is used for the computations. The signals are broadband ground displacements in the passband 0.005-0.9 Hz. The data and synthetics are normalized by the peak-to-peak amplitude, blue number in unit of 10^{-6} m.

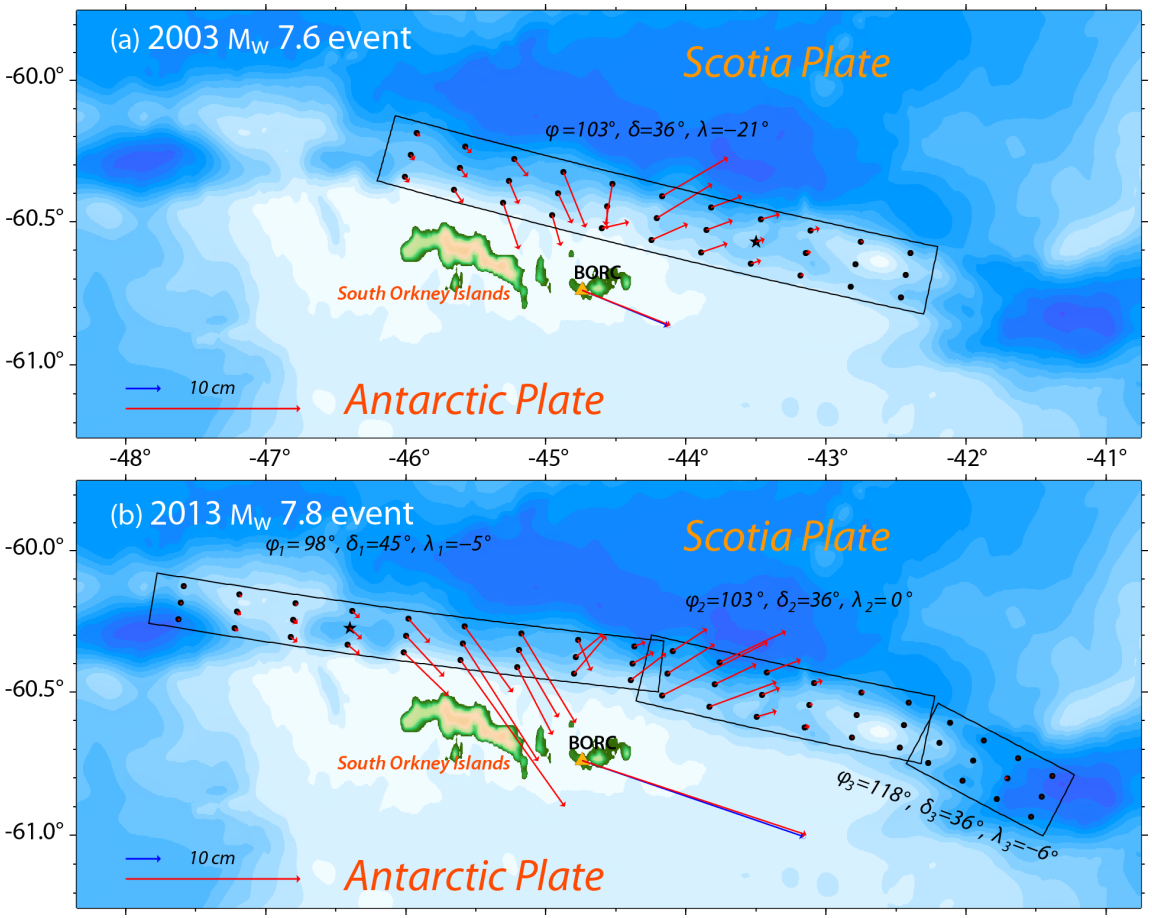

Fig. S8. Maps similar to Fig. 6, but for the final faulting geometries and slip distributions in Fig. 7, with the contribution to the BORC displacement from each subfault being shown by the red arrows on the subfault grid. The observed (blue) and predicted (red) cumulative displacement at BORC are shown.

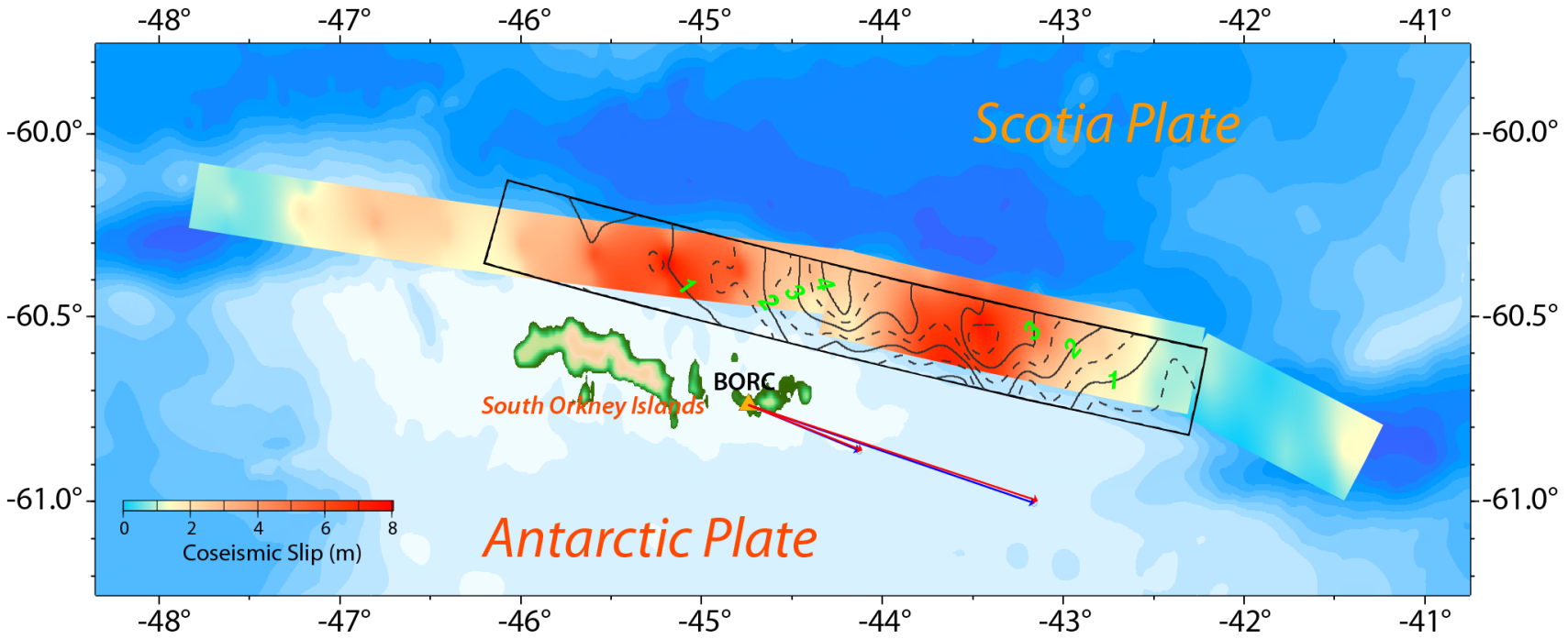

Fig. S9. Overlapping comparison of the slip distributions for the 2003 event (contour map with slip magnitudes indicated by the green numbers, and the 2013 event (color slip model). The peak slip of the 2003 event, is located in the low slip area of the 2013 event near a longitude of -44°. There is overlap of slip in the two events further to the East, but the 2013 rupture extends further eastward than the 2003 event.

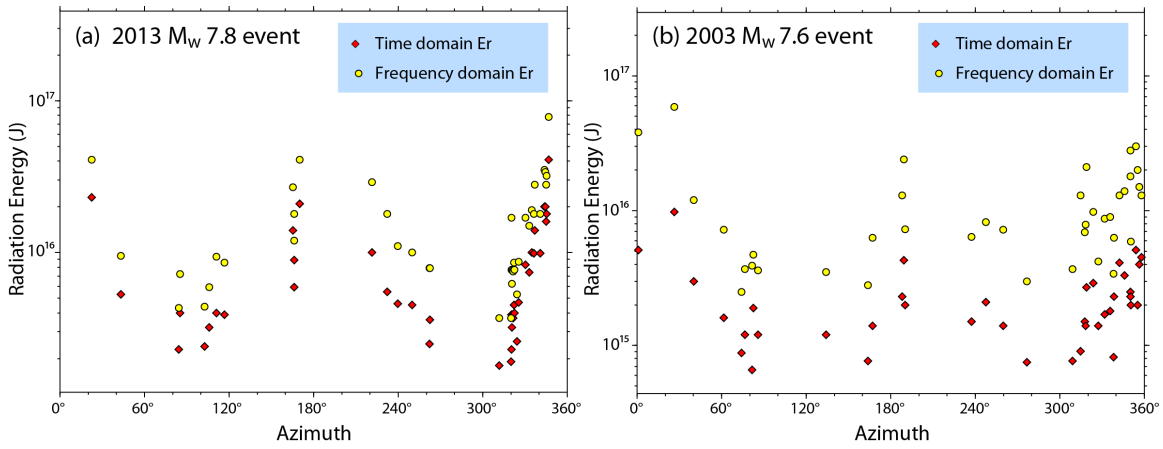

Fig. S10. Azimuthal distribution of the radiated energy estimates (Venkataraman and Kanamori, 2004) in the frequency band of ~0.05-1.5 Hz from teleseismic P wave recordings for (a) November 17, 2013 M_w 7.8 Scotia earthquake and (b) August 4, 2003 M_w 7.6 Scotia earthquake. The individual station estimates of P wave radiated energy for the 2013 event show strong azimuthal variation, typical of strike-slip events.